A Model for Buoyant Tephra Plumes Coupled to Lava Fountains With an Application to the 29th of August 2011 Paroxysmal Eruption at Mount Etna, Italy

Snee, Evie; Degruyter, Wim; Bonadonna, Costanza; Scollo, Simona; Rossi, Eduardo; Freret-Lorgeril, Valentin

JGR Solid Earth

RESEARCH ARTICLE
10.1029/2020JB021360

A Model for Buoyant Tephra Plumes Coupled to Lava Fountains With an Application to the 29th of August 2011 Paroxysmal Eruption at Mount Etna, Italy

E. Snee[1], W. Degruyter[1], C. Bonadonna[2], S. Scollo[3], E. Rossi[2], and V. Freret-Lorgeril[2]

[1]Department of Earth and Ocean Sciences, Cardiff University, Cardiff, UK, [2]Department of Earth Sciences, University of Geneva, Geneva, Switzerland, [3]Istituto Nazionale di Geofisica e Vulcanologia, Osservatorio Etneo, Catania, Italy

Key Points:

- We have developed a new integral model that accounts for the coupling between a tephra plume and a lava fountain
- The initial grain-size distribution and radius of a lava fountain control the rise height of the surrounding tephra plume
- The model can explain the relationship between the tephra plume and cone deposits and the observed plume and lava fountain height

Correspondence to:
E. Snee,
sneee@cardiff.ac.uk

Citation:
Snee, E., Degruyter, W., Bonadonna, C., Scollo, S., Rossi, E., & Freret-Lorgeril, V. (2021). A model for buoyant tephra plumes coupled to lava fountains with an application to the 29th of August 2011 paroxysmal eruption at Mount Etna, Italy. *Journal of Geophysical Research: Solid Earth*, *126*, e2020JB021360. https://doi.org/10.1029/2020JB021360

Received 17 NOV 2020
Accepted 19 APR 2021

Abstract Explosive basaltic eruptions pose significant threats to local communities, regional infrastructures and international airspace. They produce tephra plumes that are often associated with a lava fountain, complicating their dynamics. Consequently, source parameters cannot be easily constrained using traditional formulations. Particularly, mass flow rates (MFRs) derived from height observations frequently differ from field deposit-derived MFRs. Here, we investigate this discrepancy using a novel integral plume model that explicitly accounts for a lava fountain, which is represented as a hot, coarse-grained inner plume co-flowing with a finer-grained outer plume. The new model shows that a plume associated with a lava fountain has higher variability in rise height than a standard plume for the same initial MFR depending on initial conditions. The initial grain-size distribution and the relative size of the lava fountain compared to the surrounding plume are primary controls on the final plume height as they determine the strength of coupling between the two plumes. We apply the new model to the August 29, 2011 paroxysmal eruption of Mount Etna, Italy. The modeled MFR profile indicates that the field-derived MFR does not correspond to that at the vent, but rather the MFR just above the lava fountain top. High fallout from the lava fountain results in much of the erupted solid material not reaching the top of the plume. This material deposits to form the proximal cone rather than dispersing in the atmosphere. With our novel model, discrepancies between the two types of observation-derived MFR can be investigated and understood.

1. Introduction

Explosive basaltic volcanism can generate ash-rich plumes that can cause significant local and regional disruption (Andronico et al., 2015; Barsotti et al., 2010; Scollo et al., 2013). Many of these plumes are characterized by a hot inner core that is defined as a lava fountain. These lava fountains, that are defined as sustained ejections of hot pyroclasts (Taddeucci et al., 2015), can rise to hundreds of meters, or even kilometers above the volcanic vent (Calvari et al., 2018). The climactic phases of these eruptions, where the lava fountain and tephra plume co-exist, are referred to as paroxysmal eruptions (Alparone et al., 2003). Such eruptions have occurred at volcanoes including Mount Etna (Italy), Izu Oshima (Japan) and Villarrica (Chile; Calvari et al., 2018; Mannen, 2006; Romero et al., 2018). While the dynamics of ash-rich, buoyant plumes are well studied, the impact of a hotter, coarser, inner core inside the plume needs to be considered (e.g., first phase of the 2010 eruption of Eyjafjallajökull, Iceland; Kaminski et al., 2011). In this study, we focus on the interaction between lava fountains and buoyant ash-rich plumes and the implications for estimating eruption source parameters (ESPs). In particular, we investigate lava fountains coexisting with ash-rich plumes that originate from a single summit crater as opposed to long eruptive fissures.

The numerous paroxysmal eruptions at Mount Etna are characterized by lava fountains combined with ash-rich plumes. Between 2011 and 2015 Mount Etna produced more than 50 eruptions (Calvari et al., 2018; Freret-Lorgeril et al., 2018). These eruptions occurred at the summit and formed the New South East Crater; a significant build of over 200 m in just three years (Behncke et al., 2014; De Beni et al., 2015). The eruptions typically start with Strombolian activity that transitions into sustained lava fountains (Alparone et al., 2003; Behncke et al., 2014). Lava flows are commonly observed during the Strombolian activity (Behncke et al., 2014; Calvari et al., 2018). Ash emissions become sustained to form volcanic plumes (see Figure 1) that can rise up to 15 km a.s.l (above sea level) and can disperse ash over hundreds of km (Azzopardi et al., 2013; Poret, Corradini, et al., 2018; Corradini et al., 2018). Sustained activity lasts on the timescales of hours. The ash generated by Etna's explosive activity poses a threat to

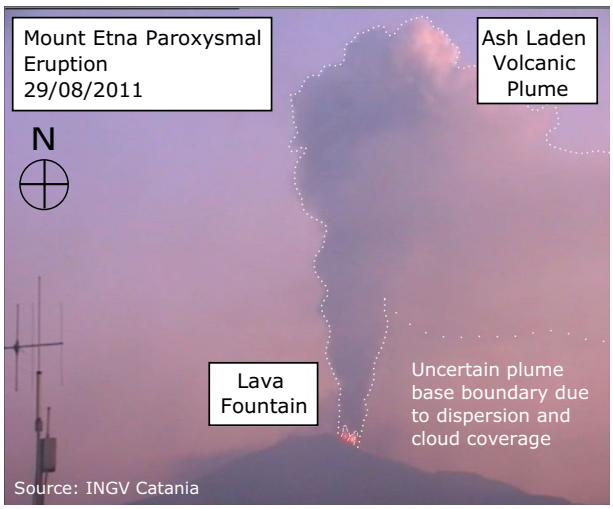

Figure 1. The August 29, 2011 eruption of Mount Etna captured from the ECV camera, located 27 km from the summit (Scollo et al., 2014). Source: INGV-OE.

airspace and local communities (Andronico et al., 2015; Horwell et al., 2017; Scollo et al., 2013). At Mount Etna, it is the responsibility of the Istituto Nazionale di Geofisica e Vulcanologia, Osservatorio Etneo (INGV-OE), to monitor Etna's eruptions to help mitigate the associated risk. Remote sensing, visual observations and modeling are used to determine the dispersion of volcanic ash (Scollo et al., 2009, 2013, 2019). Over the years, the INGV-OE has gathered a plethora of data on these types of eruptions, making Mount Etna the ideal candidate to test and validate models for such type of activity.

A key tool in understanding the dynamics of volcanic plumes are integral plume models. These are based on the theory of buoyant plumes from a maintained source formulated by Morton et al. (1956). Additional volcanological processes, such as being initially driven by momentum and particle fallout, have been applied to improve the suitability of integral plume models to volcanic plumes (Bursik, 2001; Woods, 1988; Woods & Bursik, 1991). They are used to study the relationship between ESPs and atmospheric conditions, and top rise height, neutral buoyancy height and parameter profiles (e.g., temperature, velocity) of a plume (Devenish, 2013; Girault et al., 2014; Costa, Suzuki, et al., 2016). Due to the success of using integral plume models to describe volcanic plumes, they are used operationally in volcano observatories to better determine the mass flow rate (MFR) of an eruption in real time for an observed plume height (Durig et al., 2015; Scollo et al., 2019). Nonetheless, these models have mostly been calibrated on silica-rich volcanic plumes, while their applicability to basaltic plumes requires further study.

Integral plume models have previously been applied to tephra plumes that are coupled to lava fountains through a series of adaptations. One such adaptation is the change from a circular to linear vent geometry to better model plumes from fissure fed fountains of the Laki 1783 eruption (Stothers et al., 1986; Woods, 1993). However, tephra plumes from paroxysmal eruptions can occur from a circular summit crater. Additionally, Parfitt and Wilson (1999) demonstrated the successful ability of applying an integral plume model to match independent measurements of the dynamics of a lava fountain-tephra plume system in Hawaii. By using basaltic ESPs, including a realistic coarse grain-size distribution (GSD), and accounting for dynamic disequilibrium of different particle sizes at the source (Wilson & Walker, 1987; Woods & Bursik, 1991), the behavior of a lava fountain is more accurately represented in the model. More recent studies have focused on modeling larger sub-Plinian plumes that are coupled to large lava fountains by only modeling the plume portion of the system (Glaze et al., 2017). The integral model is applied to the plume above the lava fountain and the ESPs are adapted to account for how much solid mass has been lost from the system in the lava fountain region. This is achieved by using an effective volatile content, which is determined by using a partitioning factor and the bulk volatile content of the magma (Kaminski et al., 2011). However, this approach does not explicitly consider the lava fountain and tephra plume interaction and therefore the impact of the lava fountain on plume rise is not completely determined.

We first show that the use of a standard integral model is inadequate to simulate coupled lava fountains - tephra plumes. To fully investigate the effect of a lava fountain on a volcanic plume, we therefore develop a new, 1D integral coaxial, buoyant plume model that simulates interaction between an inner, circular plume (representing the lava fountain) and an outer, annular-shaped, buoyant plume through the processes of entrainment and particle fallout. We will refer to this model as the double plume model in what follows. We then explore the effect of varying source conditions, such as the initial GSD, and the size of a lava fountain on MFR estimates with the new double plume integral model. Finally, we apply the model to the August 29, 2011 eruption of Mount Etna, where a transitional tephra plume (Scollo et al., 2019), that is, a plume only moderately affected by wind, was coupled with a lava fountain.

2. Applicability of a Standard Integral Model to Coupled Lava Fountains - Tephra Plumes

Before applying the new double plume model to plumes coupled with lava fountains from paroxysmal eruptions, we determine the suitability of a standard integral model for simulating these plumes. We use the integral model of Degruyter and Bonadonna (2012), that has been adapted to account for particle sedimentation during plume

Table 1
ESPs for MonteCarlo Simulations Using the Standard Integral Model Used in Figures 2 and 3

ESP	Standard integral model
Total MFR (kg s^{-1})	10^3–10^7
Temperature (K)	900–1,200
Velocity (m s^{-1})	75–200
Gas mass fraction	0.01–0.03
GSD	Derived from tephra deposit if available or log-normal GSD used in operational modeling

Abbreviation: MFR, mass flow rate.

rise following the approach of Ernst et al. (1996) and Bursik (2001). Hereinafter, this will be referred to as the standard integral model to distinguish from the double plume model. To explore the applicability of the standard integral model to tephra plumes that coexist with a lava fountain, we randomly sample the parameter space defined in Table 1 to invert the ESPs from the observed plume height. The ESPs that we vary include initial velocity, gas mass fraction, temperature and MFR. We treat the initial gas mass fraction and exit velocity as independent of each other and keep the entrainment coefficients in the model fixed at 0.1 and 0.5 for the radial and wind entrainment coefficients, respectively, as these are the values used in operational modeling by INGV-OE (Scollo et al., 2019) and also supported by several studies (Aubry et al., 2017; Devenish, Rooney, Webster, & Thomson, 2010; Michaud-Dubuy et al., 2020). The initial GSD used is dependent on the eruption that we are modeling. If a field-derived GSD is available, we use this GSD as the initial GSD. Otherwise, we use a log-normal GSD with a median grain-size of 0.5 phi and a standard deviation of 1.5 phi in accordance with the values used in operational modeling by INGV-OE (Scollo et al., 2019). Atmospheric conditions (wind, temperature and pressure) are determined from the ECMWF ERA Interim, Daily data sets (Dee et al., 2011) for each eruption examined in this section. In this section only, we do consider the effect of wind on the rise height of the buoyant tephra plume. We follow a similar procedure to the approach of Mastin (2014), Devenish (2016) and Scollo et al. (2019) by calculating the final plume height both in the presence of wind (Z_{wind}) and without wind ($Z_{no\ wind}$). When considering the presence of wind, the final plume height, is considered to be the sum of the center-line height and the plume radius. We choose the minimum plume height to avoid the case of a bent over plume going higher than a plume without wind

$$Z_{final} = \min(Z_{wind}, Z_{no\ wind}). \quad (1)$$

2.1. Gas-Thrust Region

We first explore the relationship between the lava fountain and the gas-thrust region of a buoyant tephra plume. A lava fountain is defined as a vertical jet of coarse material that is driven by kinetic energy and reaches its final height once this kinetic energy is completely exhausted. This height can be derived from Bernouilli's equation and is given as $U^2/(2g)$ where U is the velocity at the source and g is gravitational acceleration. This is often referred to as the ballistic height (Bonaccorso et al., 2014; Head & Wilson, 1989). In contrast, the gas-thrust region is the negatively buoyant lower region of a plume that is driven upwards by the initial momentum. Once the buoyancy becomes positive, that is, where the bulk density of the plume equates to that of the ambient density, the gas-thrust region stops and the convective region begins (Carey & Bursik, 2015). Although a lava fountain and the gas-thrust region are different, the terms have sometimes been used interchangeably. Thermal camera images at Mount Etna, show a hot core extending far above the incandescent region seen by the naked eye and this has previously been interpreted as the lava fountain (Calvari et al., 2018). The height of this thermally-saturated region, defined by different thresholds depending on the camera in question (Calvari et al., 2018), has often been equated to the gas-thrust region of the plume (Calvari et al., 2018; Vulpiani et al., 2016;). We demonstrate the clear difference between the height of the gas-thrust region and the height of the lava fountain in Figure 2. The height of the gas-thrust region is determined with the standard integral model as the height at which the modeled plume becomes less dense than the surrounding fluid (i.e., the point where the modeled plume becomes buoyant) for ESPs that reproduces the observed plume height (9–9.9 km a.s.l; Corradini et al., 2018; Freret-Lorgeril

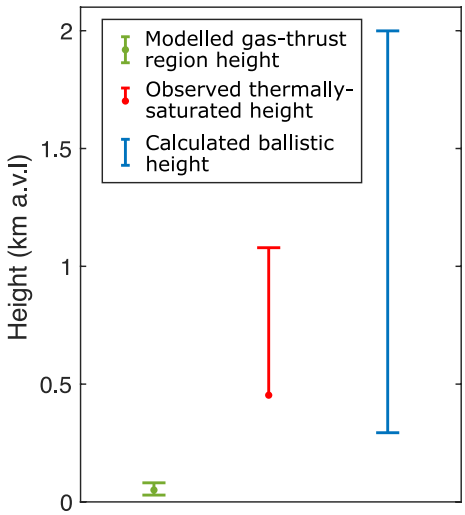

Figure 2. A comparison between the modeled gas-thrust region (green) of a buoyant tephra plume and the observed (red) thermally-saturated region for the August 29, 2011 paroxysmal eruption of Mount Etna, Italy (Calvari et al., 2018). The calculated ballistic height is also plotted (blue). The error bars are defined with the minimum, average and maximum heights (if available) to show the variability of the height of the feature in question.

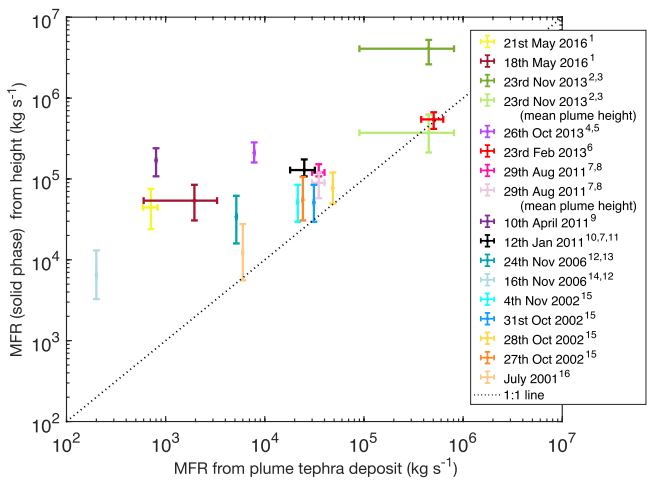

Figure 3. A comparison between the MFRs determined from the tephra deposits associated with plume sedimentation with those determined from the observed plume height, using a standard integral model, for paroxysmal eruptions of Mount Etna between 2000 and 2016, whose plume tephra deposits have been characterized. The model is that of Degruyter and Bonadonna (2012), but adapted to account for sedimentation from the plume margins. Data sources: [1] Edwards et al. (2018), [2] Andronico et al. (2015), [3] Corradini et al. (2016), [4] Andronico et al. (2018), [5] de Michele et al. (2019), [6] Poret, Costa, et al. (2018), [7] Corradini et al. (2018), [8] Freret-Lorgeril et al. (2021), [9] Andronico, Scollo, Cristaldi, and Lo Castro (2014), [10] Calvari et al. (2011), [11] Andronico, Spinetti, et al. (2009), [12] Andronico, Scollo, Lo Castro, et al. (2014), [13] Andronico, Scollo, et al. (2009), [14] Andronico et al. (2008) [15] Scollo et al. (2007).

et al., 2021) of the August 29, 2011 paroxysmal eruption at Mount Etna. The ballistic heights range between 287 and 2,039 m due to the velocity range in the parameter space. These are consistent with the observed range from thermal camera-imaging by Calvari et al. (2018), while the gas-thrust region is significantly lower. This is further supported by recent analyses that have decoupled the gas-thrust region from the vertical ballistic region detected by radar (Mereu et al., 2020). Hence, a standard integral model does not capture the lava fountain height appropriately.

2.2. Mass Flow Rate

Discrepancies exist between the initial MFR determined from the plume tephra deposit and those calculated from the plume height (Figure 3). We have again used the standard integral model to show that the MFR calculated from the maximum plume height is greater, by up to two orders of magnitude, than those determined from the field deposits for Etna eruptions between 2000 and 2016. This suggests that the well-established relationship between plume height and initial MFR (Degruyter & Bonadonna, 2012; Girault et al., 2014; Gouhier et al., 2019; Mastin et al., 2009; Sparks et al., 1997; Woodhouse et al., 2013) could differ for paroxysmal eruptions at Mount Etna. In the majority of these calculations, the maximum, rather than the mean plume height, was considered owing to a lack of available data. However, for the August 29, 2011 and the November 23, 2013 eruptions of Mount Etna, we also plot the results when using the mean plume height. Whilst this has partially resolved the conundrum for the November 23, 2013 eruption, the discrepancy still exists for the August 29, 2011 eruption. These discrepancies highlight the need for further investigation of tephra plumes that are coupled to lava fountains and how they differ from more typical plumes. As a result, we develop a model that can be used to simultaneously capture the lava fountain and tephra plume height and relate these heights to the field deposit.

3. Model

3.1. Description

We present an integral model of a coaxial double plume. The underlying principles follow those of commonly used integral plume models, which are based on the buoyant plume theory developed by Morton et al. (1956). The distinctive feature is to explicitly treat the dynamics of a dense core at the source and how it feeds an ash-rich outer rim through mass, momentum, and enthalpy exchange. Double plume models, using buoyant plume theory, are used to better represent the complex characteristics of a plume without drastically increasing the computational expense. They are commonly used to better represent turbulence in a plume by having a counter-flowing plume surrounding the rising plume (Bloomfield & Kerr, 2000; Mcdougall, 1978, 1981). A counter-flowing double plume model has been applied to volcanic plumes in a still atmosphere and can better capture complex flow patterns of a volcanic plume and the MFR in the umbrella region of a volcanic plume (Devenish & Cerminara, 2018). Such models have also been applied to submarine eruption plumes (Mittal & Delbridge, 2019). The study of coaxial plumes ranges from theoretical studies to application to plumes from cooling towers (Li & Flynn, 2020; Li et al., 2018: Morton, 1962). The model that we present takes inspiration from the coaxial models in the literature (Devenish & Cerminara, 2018; Li et al., 2018) to create a coaxial double plume model for a tephra plume that is coupled to a lava fountain.

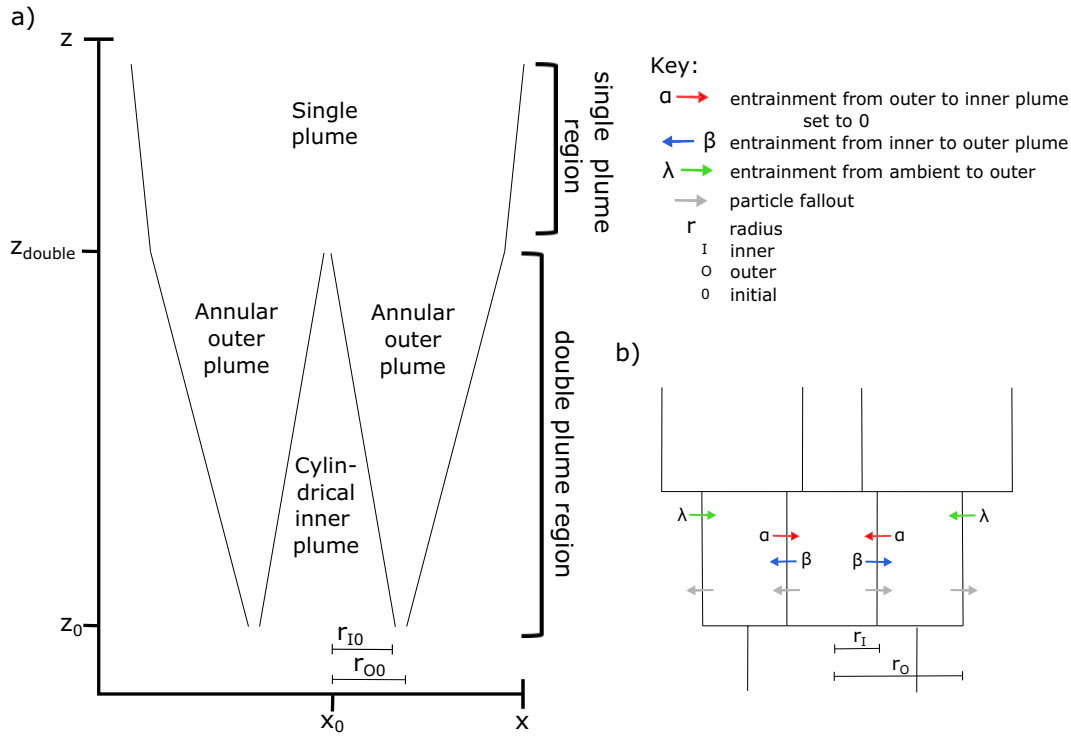

Figure 4. (a) Schematic of the double plume model that shows the coordinate system and what each part of the model represents. (b) Detailed schematic of the control volume of the double plume model. The coupling of the inner and the outer plumes is highlighted by the arrows.

We assume that the plume is composed of two regions; the double plume region where a lava fountain and plume coexist, which transitions into a single plume at higher altitudes (Figure 4). The double plume region is treated as two separate plumes that are coupled; an inner circular plume that is surrounded by an outer annular plume, which hereinafter will be referred to as the inner plume and the outer plume. The inner plume is representative of the hot inner core (the lava fountain) and the outer plume is the ash laden buoyant plume observed in coupled lava fountain–tephra plume eruptions. This allows for a better description of the different source conditions between a lava fountain and a tephra plume compared to a standard integral model. The initial MFR is split at the source into two portions; one for the inner plume (M_{i0}) and one for the outer plume (M_{o0}). We quantify the mass partitioning through the ratio $\varepsilon = M_{i0}/(M_{i0} + M_{o0})$; the greater the value of ε the greater the relative proportion of MFR in the inner plume. At the height where the rise velocity or the solid phase MFR of the inner plume becomes negligible, that is, top of the lava fountain, the plume transitions to a single plume description. The initial source conditions of the inner and the outer plume are independent of each other. The initial gas mass fraction and velocity of each plume are also independent of each other as we do not impose a choked vent (Woods & Bower, 1995). A common assumption for large, ash-rich silicic eruptions is to assume choked vent conditions, whereby the exit velocity is equal to the sound velocity of the mixture (e.g., Girault et al., 2014). We do not impose this restriction here as this condition is not necessarily met for eruptions with low initial MFR that co-exist with lava fountains. A schematic of the model setup can be seen in Figure 4a. To simplify the problem to one-dimension, we assume the following.

1. The plume rise timescale for both the inner and the outer plume is less than the timescale of mass injection and, therefore, the plume is sustained
2. The turbulent eddy turnover time is less than the timescale of plume rise
3. The rate of entrainment into the plume is proportional to the velocity of the plume
4. The pressure inside the plume is in equilibrium with the atmospheric pressure
5. Plume properties are self-similar at a given height for which we assume a top-hat profile
6. The vent is circular

We consider the plume to consist of three phases – dry air, water vapor and solid mass. These phases are exchanged between the inner and outer plumes, and the surrounding atmosphere via entrainment and particle fallout. Figure 4b shows the direction and the type of coupling that can happen between the atmosphere, the inner and the outer plume. The plume velocities are related to the rate of entrainment via a set of entrainment coefficients. The rate of entrainment from the atmosphere to both the outer plume and the single plume is described by λ and χ. α and β are used to determine the rate of entrainment from the outer plume to the inner plume, and vice-versa, in the double plume region of the model. We follow the same notation for the entrainment coefficients as Bloomfield and Kerr (2000), who determined the values of α, β, and λ as 0.085, 0.147, and 0.147, respectively, for a double plume from the fitting of numerical models to small-scale experiments. The entrainment velocities are calculated as shown by Equations 2–4 that have been modified to take into account large density difference between the plume and the surrounding fluid (Devenish & Cerminara, 2018; Morton, 1965; Ricou & Spalding, 1961; Rooney & Linden, 1996):

$$\mu_\lambda = u_o \lambda \left(\frac{\rho_{oB}}{\rho_{aB}} \right)^{0.5}, \tag{2}$$

$$\mu_\alpha = (u_I - u_o)\alpha \left(\frac{\rho_{IB}}{\rho_{oB}} \right)^{0.5}, \tag{3}$$

$$\mu_\beta = u_o \beta \left(\frac{\rho_{oB}}{\rho_{IB}} \right)^{0.5}, \tag{4}$$

where u is the plume velocity and ρ is the bulk plume density. Table 3 defines the subscripts. We use the values of 0.147 and 0.147 for the β and λ, respectively, from Bloomfield and Kerr (2000) in the double plume region of the double plume model. We further assume that re-entrainment of solid particles does not occur, and gas phases are not entrained into the inner plume (α is set to 0). This results in a decrease of the MFR of the inner plume with height, and therefore also a decrease in plume radius with height, which matches the observed structure of lava fountains.

The conservation of mass, momentum and specific enthalpy are solved in the model for the inner, outer and single plume. The definition of each variable is listed in Table 2.

3.2. Governing Equations of the Double Plume Region

The conservation of mass flow rate for dry air (d) and water vapor (v) for the inner plume (denoted by subscript I, see Table 3) are defined by Equations 5 and 6, where the left-hand side is the rate of mass flow rate change with height of the respective phase. The sink and sources compose the right-hand side of the equations. These are the same for both the dry air and vapor phase. The first term is the source of the respective phase of material entrained from the surrounding outer plume, while the second term is the MFR loss of the respective phase from the inner plume due to entrainment to the outer plume.

$$\frac{d(\rho_{Id} u_I r_I^2)}{dz} = 2\rho_{Od}\mu_\alpha r_I - 2\rho_{Id}\mu_\beta r_I \tag{5}$$

$$\frac{d(\rho_{Iv} u_I r_I^2)}{dz} = 2\rho_{Ov}\mu_\alpha r_I - 2\rho_{Iv}\mu_\beta r_I \tag{6}$$

In the inner plume, the change of the solid MFR is described by Equation 7. The change of the MFR of the solid phase is described by amount of solid MFR lost from particle fallout. The conservation of mass flow rate for the solid phase is solved for each grain-size in the model.

$$\frac{d(\rho_{Is} u_I r_I^2)}{dz} = -\sum_{i=1}^{n_i} p_{Gauss} \frac{M_{Isi}}{r_I} \tag{7}$$

Table 2
Definitions of Symbols

Symbol	Definition	Value	Units
Z	vertical coordinate	–	m
γ	radius	–	m
U	velocity	–	m s^{-1}
ρ_B	bulk density	–	kg m^{-3}
ρ_l	density of liquid phase in plume	1,000	kg m^{-3}
ρ_s	density of solid phase in plume	2,000	kg m^{-3}
μ	entrainment velocity/rate of entrainment	–	ms^{-1}
W	settling velocity of a particle	–	m s^{-1}
$r_e nv$	radius of the support envelope	–	m
g	gravitational acceleration	9.81	m s^{-2}
C_B	bulk specific heat capacity	–	J kg^{-1} K^{-1}
C_B	specific heat capacity of dry air	998	J kg^{-1}
C_v	specific heat capacity of water vapor	1,952	J kg^{-1}
C_s	specific heat capacity of solids	1,250	J kg^{-1} K^{-1}
θ	temperature	–	K
n	mass fraction	–	–
ε	mass partition ratio between inner and outer plume	–	–
M	mass flow rate	–	kg s^{-1}
E	enthlapy flow rate	–	J s^{-1}
P	pressure (assume plume is at pressure equilibrium with the atmosphere)	–	Pa
R_g	specific gas constant	–	J kg^{-1} K^{-1}
R_d	specific gas constant of dry air	287	J kg^{-1}
R_v	specific gas constant of water vapor	461	J $kg^{-1}K^{-1}$
P	probability of particle fallout for entraining plume	0.27	–
p_{gauss}	probability of particle fallout for plume that does not entrain	–	–
d	diameter of grain-size	–	m
v	dynamic viscosity	–	kg m s^{-1}
α	entrainment coefficient describing entrainment from outer to inner plume	0	–
β	entrainment coefficient describing entrainment from inner to outer plume	0.147	–
λ	entrainment coefficient describing entrainment from ambient to outer plume	0.147	–
X	entrainment coefficient describing entrainment from ambient to single plume	0.1	–
H_1	height of the tropopause	11,000	m
H_2	height of the stratosphere	20,000	m
ω_{trop}	temperature gradient in the troposphere	−0.0065	K m^{-1}
ω_{strat}	temperature gradient in the stratosphere	−0.002	K m^{-1}
θ_{ao}	initial temperature of the atmosphere	280	K

Table 3
Definitions of Subscripts

Subscript type	Subscript symbol	Definition
Location	O	Outer plume
	I	Inner plume
	A	Atmosphere
Phase	D	Dry air
	V	Water vapor
	S	Solid
	B	Bulk
Entrainment	α	Entrainment from outer to inner plume
	β	Entrainment from inner to outer plume
	λ	Entrainment from ambient to outer plume
	χ	Entrainment from ambient to single plume
Grain-size	i	Grain-size class i

We consider grain-sizes from −9 phi to 10 phi, with a spacing of half a phi, where phi is defined as $\log_2 D$ with D being the diameter of the particle in meters. Details of the description of particle fallout from the inner plume can be found further in Section 3.4.

For the outer plume (denoted by subscript O) in the double plume region, the processes that control the change in mass flow rate are the same as in the inner plume. An additional entrainment term is present in the conservation of mass flow rate for dry air and water vapor (third term in Equations 8 and 9) for the entrainment of mass from the atmosphere into the outer plume. An additional term is also present in the conservation of mass flow rate of the solid phases as a source term for the particles that move from the inner plume into the outer plume (second term, Equation 10).

$$\frac{d(\rho_{Od}u_O(r_O - r_I)^2)}{dz} = -2\rho_{Od}\mu_\alpha r_I + 2\rho_{Id}\mu_\beta r_I + 2\mu_\lambda r_O \rho_{ad} \tag{8}$$

$$\frac{d(\rho_{Ov}u_O(r_O - r_I)^2)}{dz} = -2\rho_{Ov}\mu_\alpha r_I + 2\rho_{Iv}\mu_\beta r_I + 2\mu_\lambda r_O \rho_{av} \tag{9}$$

$$\frac{d(\rho_{Os}u_O(r_O - r_I)^2)}{dz} = -\sum_{i=1}^{n_i} p\frac{w_{Osi}M_{Osi}}{u_O r_O} + \sum_{i=1}^{n_i} p_{Gauss}\frac{M_{Isi}}{r_I} \tag{10}$$

The change in the momentum flow rate is described by Equation 11 for the inner plume and by Equation 12 for the outer plume. The momentum flow rate is increased from the material added to the plumes via entrainment (for dry air and water vapor) and from buoyancy. For the inner plume, these are described by the first, second and fifth term in Equation 11, respectively, and by the third, fourth, and fifth term in Equation 12, respectively. The outer plume has the additional source of momentum from the solid particles that fall from the inner to the outer plume depending on the relative settling and plume velocity (seventh term, Equation 12). The loss of momentum flow rate from the plumes is via the processes of entrainment of dry air and water vapor and particle fallout. These refer to the third, fourth and sixth term in Equation 11 for the inner plume and the first, second, and sixth term in Equation 12 for the outer plume.

$$\begin{aligned}\frac{d(\rho_{IB}r_I^2u_I^2)}{dz} = {} & 2\rho_{Od}\mu_\alpha r_I u_O + 2\rho_{Ov}\mu_\alpha r_I u_O - 2\rho_{Id}\mu_\beta r_I u_I - 2\rho_{Iv}\mu_\beta r_I u_I \\ & + g(\rho_{aB} - \rho_{IB})r_I^2 + u_I\frac{d(\rho_{Is}u_I r_I^2)}{dz}\end{aligned} \tag{11}$$

$$\begin{aligned}\frac{d(\rho_{OB}(r_O - r_I)^2u_O^2)}{dz} = {} & -2\rho_{Od}\mu_\alpha r_I u_O - 2\rho_{Ov}\mu_\alpha r_I u_O + 2\rho_{Id}\mu_\beta r_I u_I + 2\rho_{Iv}\mu_\beta r_I u_I \\ & + g(\rho_{aB} - \rho_{OB})(r_O - r_I)^2 + u_O\frac{d(\rho_{Os}u_O(r_O - r_I)^2)}{dz} \\ & - u_I\frac{d(\rho_{Is}u_I r_I^2)}{dz}\end{aligned} \tag{12}$$

The left-hand side of Equations 13 and 14 shows the variation with respect to height of the enthalpy flow rate of the volcanic mixture of the inner and outer plume, respectively. As in the conservation of momentum flow rate for both the inner and the outer plumes (Equations 11 and 12), the change in the enthalpy is caused by the enthalpy gained from the addition of mass flow rate into a plume via entrainment and particle fallout. While the enthalpy flow rate is reduced by entrainment of material from the plume, change due to conversion to gravitational potential energy and particle fallout.

$$\begin{aligned}\frac{d(\rho_{IB}r_I^2u_IC_{IB}\theta_I)}{dz} = {} & 2\rho_{Od}\mu_\alpha r_I C_d\theta_O - 2\rho_{Id}\mu_\beta r_I C_d\theta_I + 2\rho_{Ov}\mu_\alpha r_I C_v\theta_O \\ & - 2\rho_{Iv}\mu_\beta r_I C_v\theta_I - \rho_{IB}u_I r_I^2 g\frac{\rho_{aB}}{\rho_{IB}} + C_s\theta_I\frac{d(\rho_{Is}u_I r_I^2)}{dz}\end{aligned} \tag{13}$$

$$\frac{d(\rho_{OB}(r_O - r_I)^2 u_O C_{OB}\theta_O)}{dz} = -2\rho_{Od}\mu_\alpha r_I C_d\theta_O + 2\rho_{Id}\mu_\beta r_I C_d\theta_I + 2\rho_{ad}\mu_\lambda r_O C_d\theta_a - 2\rho_{Ov}\mu_\alpha r_I C_v\theta_O + 2\rho_{Iv}\mu_\beta r_I C_v\theta_I + 2\rho_{av}\mu_\lambda r_O C_v\theta_a - \rho_{OB}u_O(r_O - r_I)^2 g\frac{\rho_{aB}}{\rho_{OB}} - C_s\theta_I\frac{d(\rho_{Is}u_I r_I^2)}{dz} + C_s\theta_O\frac{d(\rho_{Is}u_O(r_O - r_I)^2)}{dz} \quad (14)$$

The total mass flow rate and mass fractions for each phase (both for the inner or the outer plumes) are given by Equations 15 and 16 to 18, respectively,

$$M = M_d + M_v + M_s \quad (15)$$

$$n_d = \frac{M_d}{M_d + M_v + M_s} \quad (16)$$

$$n_v = \frac{M_v}{M_d + M_v + M_s} \quad (17)$$

$$n_s = \frac{M_s}{M_d + M_v + M_s} \quad (18)$$

where M_d, M_v and M_s are the mass flow rates of the dry air, water vapor and solid phases.

The material properties of the plume are described by the following constitutive equations, which once again apply to both the inner and outer plume. The mixture heat capacity (C_B) is

$$C_B = \frac{M_d C_d + M_v C_v + M_s C_s}{M_d + M_v + M_s}. \quad (19)$$

From this, the plume temperature (θ) can be found from

$$\theta = \frac{1}{C_B}\frac{E}{M}, \quad (20)$$

where E is the enthalpy flow rate.

The bulk density of the plume (Equation 23) is calculated from the bulk gas constant (Equation 21) and the density of the gas phase mixture in the plume (Equation 22) using the ideal gas law.

$$R_g = \left(\frac{n_v}{n_v + n_d}R_v\right) + \left(\frac{1 - n_v}{n_v + n_d}R_d\right) \quad (21)$$

$$\rho_g = \frac{P}{R_g\theta} \quad (22)$$

$$\rho_B = \left(\frac{(n_v + n_d)}{\rho_g} + \frac{n_s}{\rho_s}\right)^{-1} \quad (23)$$

We use the ode15s solver in MATLAB to solve the governing equations for the inner and outer plume together to be able to include the entrainment of the inner plume to the outer and vice-versa (Shampine & Reichelt, 1997; Shampine et al., 1999). The ordinary differential equations (ODEs) solved are Equations 5–14 along with the closure Equations 15–23.

3.3. Transition From the Double Plume to the Single Plume

The initial double plume of the model stops when the inner plume velocity approaches 0 m s^{-1}. The inner plume is stopped earlier if the solid MFR in the inner plume becomes negligible. Additionally, in the case where a given

grain-size is no longer supported by the inner plume, the simulation is paused, and the corresponding MFR of that grain-size is removed from the system. Associated momentum and enthalpy related to the fallout are also removed. The system of equations is then continued from the height where it was halted. When either of these conditions are met, the inner plume disappears, and the outer plume governing equations change to those of just a single plume.

Two end member situations exist for the treatment of any solid material remaining in the inner plume once it has stopped. The solid phase MFR in the inner plume can either be completely removed from the system or can be added to the single plume. However, due to the dependence on grain-size, it is unlikely that the total solid phase MFR of all sizes present in the plume would be incorporated into the single plume. Therefore, a support envelope approach can be implemented, whereby grain-sizes that can no longer be supported by the plume are removed (Carey & Sparks, 1986).

Equations 24–28 are the governing equations of the single plume model.

$$\frac{d(\rho_d u r^2)}{dz} = 2\mu_\chi r \rho_{ad} \tag{24}$$

$$\frac{d(\rho_v u r^2)}{dz} = 2\mu_\chi r \rho_{av} \tag{25}$$

$$\frac{d(\rho_s u r^2)}{dz} = \sum_{i=1}^{n_i} - p\frac{w_{si} M_{si}}{ur} \tag{26}$$

The rate of mass flow rate change in the single plume is governed by the entrainment of the ambient fluid (right-hand side, Equations 24 and 25) and particle fallout (right hand-side, Equation 26). Subsequently, the rate of momentum flow rate change is due to particle fallout, as well as buoyancy (2nd and 1st terms, Equation 27, respectively). We describe the rate of entrainment from the ambient into the single plume region as $\mu_\chi = u\chi\left(\frac{\rho_B}{\rho_{aB}}\right)^{0.5}$, where χ is the entrainment coefficient describing the proportionality between the entrainment rate and plume velocity and is equal to 0.1 (Degruyter & Bonadonna, 2012; Devenish, Rooney, Webster, & Thomson, 2010; Morton et al., 1956).

$$\frac{d(\rho_B r^2 u^2)}{dz} = g(\rho_{aB} - \rho_B) r^2 + u\frac{d(\rho_s u r^2)}{dz} \tag{27}$$

In a similar suit as Equation 27, the rate of enthalpy flow rate change is controlled by the change in mass flow rate (entrainment, 1st–2nd term, and particle fallout, 4th term, in Equation 28) and conversion to gravitational potential (3rd term, Equation 28).

$$\frac{d(\rho_B r^2 u C_B \theta)}{dz} = 2\mu_\chi r \rho_{ad} c_d \theta_a + 2\mu_\chi r \rho_{av} c_v \theta_a - \rho_B u r^2 g\frac{\rho_{aB}}{\rho_B} + C_s \theta\frac{d(\rho_s u r^2)}{dz} \tag{28}$$

This system of governing equations, along with the closure Equations 15–23, are solved with the ode45 MATLAB solver and terminate when the plume velocity approaches 0 m s^{-1}.

3.4. Particle Sedimentation

To account for sedimentation from the margins of a volcanic plume, we follow the method described in Bursik (2001), Girault et al. (2014) and Girault et al. (2016). The conservation of mass flow rate of the solid phase of a buoyant plume (Equations 10 and 26) contains an additional sedimentation term to account for the loss of the solid phase MFR from the plume. The loss of particles from a plume is assumed to be proportional to the MFR of particles (Ernst et al., 1996; Woods & Bursik, 1991) and can be mathematically described for each grain-size class (i) as

$$\frac{dM_{Mi}}{dz} = -p\frac{M_{si}}{r}\frac{w_i}{u}, \tag{29}$$

where u is the velocity of the plume, r is the plume radius and M_s is the MFR of the solid phase (s) at grain-size i at height z. p is defined as the probability of particle fallout from the margins of a plume. This has been previously determined from laboratory experiments and modeling as 0.27 for buoyant plumes (Ernst et al., 1996). The final parameter required to calculate the change in MFR associated with a grain-size at a given height is the settling velocity of the grain-size (w_i). As the behavior of settling particles is described by different settling laws in different flow regimes, the settling velocity for a given spherical grain-size is dependent on the Reynolds number as given by Bonadonna et al. (1998) and Bonadonna and Phillips (2003).

$$\left.\begin{array}{ll} \sqrt{\dfrac{3.1 d_i g(\rho_s - \rho_B)}{\rho_B}} & \text{for} \quad Re_i \geq 500 \\ d_i \left(\dfrac{4 g^2 (\rho_s - \rho_B)^2}{225 \nu \rho_B} \right)^{\frac{1}{3}} & \text{for} \quad 6 \leq Re_i \leq 500 \\ \dfrac{d_i^2 g(\rho_s - \rho_B)}{18\nu} & \text{for} \quad Re_i \leq 6 \end{array}\right\} = w_i \tag{30}$$

The particle Reynolds number is calculated as $Re_i = (d_i w_i \rho_B / \nu)$ where d_i is the diameter of a spherical particle, w_i is the settling velocity of the particle of size i and ν is the dynamic viscosity of the fluid the particle is settling in. We choose to follow the approach of Woods and Bursik (1991) and use the ρ_B in the calculation of the Reynolds number and in Equation 30. This is because the lava fountains and dense tephra plumes in this study are particle-dense and consist of large particles. As a result, the surrounding clasts contribute to the drag exerted on other particles in the plume whilst the fluid displaced by a particle in the plume is likely to be a mixture of the solid and gas phases.

In the case of a lava fountain, we assume that the entrainment of the gas phases from the outer to the inner plume is negligible such that $\alpha = 0$. This causes the radius of the inner plume to reduce with height, which agrees with visual observations. This change in radius geometry results in the sedimentation scheme of Ernst et al. (1996) not being applicable to the inner plume as it would result in no fallout. The Ernst et al. (1996) sedimentation scheme also assumes that the solid particles are fully coupled to the gas. As the GSD of the material composing lava fountains are coarse, this is not a valid assumption. Instead, we use a new method to determine how much MFR is lost from the inner plume from particle fallout based on the particle settling velocity and the Gaussian plume velocity profile. We adapt the approach of Carey and Sparks (1986) to determine when a given grain-size is no longer supported by the plume – the support envelope. The ratio between the area under the Gaussian velocity profile and the area under the Gaussian velocity profile where a clast is no longer supported by the plume is calculated (Equation 31). This replaces the geometrical term and the velocity ratio in Equation 29 as p_{Gauss}.

$$\frac{dM_{si}}{dz} = -p_{Gauss} \frac{M_{si}}{r}, \tag{31}$$

where $-p_{Gauss}$ is

$$-p_{Gauss} = 1 - \mathrm{erf}\left(2 \frac{r_{env}}{r} \right) \tag{32}$$

with r_{env} being the radius of the support envelope, which is calculated as follows (Rossi et al., 2019):

$$r_{env} = \frac{r_i}{\sqrt{2}} \ln \left(\frac{u_i}{w_i} \right)^{0.5}. \tag{33}$$

The addition of the solid phase material to the outer plume is dependent on the Gaussian center-line velocity of the outer plume and the settling velocity of the grain-size. We use the Gaussian center-line velocity as that is the highest velocity within the plume. If the Gaussian center-line velocity is greater than the settling velocity of a particle, the MFR of that particular size can be supported by the outer plume. The MFR, along with the associated momentum and enthalpy flow rates, is added to the outer plume. Conversely, if the settling velocity of a given

particle size is greater than that of the Gaussian center-line velocity, the mass, momentum and enthalpy related to it are removed from the whole system. This can be turned on or off in the double plume model.

3.5. Coupling Between the Inner and Outer Plumes

The interaction between the two regions of the double plume depends on the degree of coupling between these two flows. Coupling between the lava fountain and the tephra plume is quantified by the amount of mass, momentum and enthalpy that is exchanged between the two. One way this occurs is via entrainment, where gas can be entrained from the ambient to the tephra plume, from the tephra plume to the lava fountain and from the lava fountain to the tephra plume. This mechanism of coupling has been well studied and parameterized for single buoyant plumes (Morton et al., 1956). For coaxial integral plume models, entrainment coefficients have been defined by Bloomfield and Kerr (1998); Bloomfield and Kerr (2000) and Devenish, Rooney, and Thomson (2010). Another process that allows for coupling between the lava fountain and the tephra plume is particle fallout. Material falling from the lava fountain can potentially enter the tephra plume. If no coupling is present, the plumes behave independently of each other and plume dynamics will be very similar to that of a single plume. However, observations suggest a certain level of coupling is present.

The extent of coupling between tephra plumes and lava fountains via particle fallout is not fully understood. Observations of tephra plumes above lava fountains in Hawaii show that wind can affect the finest particle (Head & Wilson, 1989). In contrast, the lava fountains at Mount Etna are characterized by much larger quantities of ash, which co-exist with a lava fountain rather than only originating from above it (Figure 1). Additionally, during strong winds, the central portion of the lava fountain appears to not be significantly affected by wind, while the tephra plume can be bent in the direction of the wind. However, a correlation has been suggested between the height of the lava fountain and the height of the volcanic plume (Calvari et al., 2018). Further research is required to understand the extent and the impact of different levels of coupling between a lava fountain and a tephra plume.

To be able to explore the potential range of coupling and its impact on plume dynamics, we examine two end-member scenarios of coupling between the inner and outer plumes due to solid mass transfer. For both scenarios, the inner and outer plumes interact by gas being entrained from the inner to the outer plume. Particle fallout from the inner plume is added to the outer plume if the settling velocity of a given size is lower than the Gaussian center-line velocity of the outer plume for both scenarios. These scenarios are the following:

1. Fully coupled – Any solid phase MFR remaining in the inner plume once it has stopped is added to the single plume region depending on the ratio between the settling velocity and the outer plume center-line velocity. The MFR related to the gas phases left in the inner plume once it has stopped are also added to the start of the single plume region.
2. Moderately coupled – Any solid phase MFR remaining in the inner plume once it has stopped is not added to the single plume region source, corresponding to the solid MFR sedimenting to the ambient and being removed from the plume system. The MFR related to the gas phases left in the inner plume once it has stopped are not added to the start of the single plume region.

3.6. Atmospheric Conditions

The atmospheric conditions that are used in the model include the pressure, density and temperature. We assume the atmosphere is only composed of dry air and there is no humidity. Wind is not accounted for. Unless otherwise specified, we use a representative temperature profile of standard atmosphere in an intermediate climate as defined by Woods (1988),

$$\left.\begin{array}{rll} \theta_{a0} - \omega_{trop} z & \text{for} & z \le H_1 \\ \theta_{a0} - \omega_{trop} H_1 & \text{for} & H_1 \le z \le H_2 \\ \theta_{a0} - \omega_{trop} H_1 + \omega_{strat}(z - H_2) & \text{for} & z \ge H_2 \end{array}\right\} = \theta_a, \tag{34}$$

where θ_{a0} is the initial atmospheric temperature, H_1 and H_2 are the height of the tropopause and the height of the stratosphere, respectively. ω_{strat} and ω_{trop} are the temperature gradient in the troposphere and the stratosphere,

respectively. These are set to the same values used by Woods (1988). The specific heat capacity (C_{aB}) of the atmosphere is equal to C_d, the specific heat capacity of dry air, as we do not consider the humidity and vapor phase of the atmosphere. Following the same assumption, ρ_{aB} and ρ_{ad} is given in Equation 35 by using the ideal gas law. The atmospheric hydrostatic pressure is described as

$$\rho_{aB} = \rho_{ad} = \frac{P}{R_d \theta_a}, \tag{35}$$

$$\frac{dP}{dz} = -g\rho_{aB}. \tag{36}$$

4. Results

4.1. The Impact of a Lava Fountain on Plume Rise

We present results on the impact of a hotter, coarser-grained inner core, that does not entrain surrounding gas phases, on the overall rise of a volcanic plume. We compare results from the double plume model, where the initial condition of the inner plume resembles the characteristics of a lava fountain, to those of a plume where a lava fountain is not present. The latter is modeled using the standard integral model. The ESPs and atmospheric conditions used are identical to those used for the double plume model.

We randomly sample a parameter space that consists of initial velocity, temperature, gas mass fraction, GSD, MFR and partition coefficient (ε), to assess the impact of a lava fountain on plume height. The ranges for each variable are listed in Table 4a; Glaze et al., 2017; Métrich & Rutherford, 1998;; Métrich et al., 2004; Parfitt & Wilson, 1999; Poret, Costa, et al., 2018; Spilliaert et al., 2006). However, we impose that the inner plume is always hotter, coarser-grained and contains a lower initial gas mass fraction than the outer plume, mimicking lava fountain characteristics (Parfitt, 1998). The vent height is set at 0 m a.s.l. As we do not imply choked vent conditions, we allow the initial velocity to vary, independently of the initial gas fraction, between the values of 75 and 200 m s^{-1}. This range agrees with average velocity estimates of tephra plumes that are coupled to lava fountains as determined by radar (Freret-Lorgeril et al., 2018). By allowing the initial source parameters to vary over wide ranges and independently of each other, we can explore the whole range of potential implications of a lava fountain on the rise of a tephra plume.

Figure 5 shows the relationship between the initial MFR and the overall plume height in a still standard atmosphere in an intermediate climate. The MFR for the double plume model refers to the combined MFR of both the inner and outer plumes at the vent. The two double plume scenarios are shown by the colored markers whilst the standard integral model is also plotted (black markers). Regardless of whether the lava fountain and tephra plume are moderately or fully coupled (blue and red markers respectively, Figure 5), a plume coupled to a lava fountain can reach a greater variation of heights than the standard integral model for a given initial MFR. This is indicated by an r^2 of 0.986 for the double plume model (both scenarios) compared to an r^2 of 0.996 for the standard integral model output for the fitting of a power law to the MFR as a function of height. The overall trend between the two coupling scenarios of models is the same. The variation in the initial source parameters allows for a wider range of heights than a plume surrounding a lava fountain can reach compared to the standard integral model for the same initial MFR. This indicates the source conditions are an important control of plume height of tephra plumes coupled with lava fountains. However, we do see for a higher initial MFR, a plume coupled to a lava fountain can generally reach greater heights than for a plume without a lava fountain. For a plume coupled to a lava fountain with a high initial MFR, the tephra plume could support a greater proportion of the fallout from the lava fountain. The mass partitioning and the GSD introduce two important new degrees of freedom compared to the standard integral model. We explore these separately in the next sections to further investigate their control on plume rise compared to a plume without a lava fountain.

4.1.1. Sensitivity of Plume Rise to the GSD of the Lava Fountain

The effect of the initial GSD of the lava fountain (i.e., the inner plume) on plume rise is important to understand. First, this is because the GSD of a lava fountain is a major characteristic and distinguishes it from typical tephra plumes (Mueller et al., 2019; Parfitt, 1998; Parfitt & Wilson, 1999). Second, GSD is a first order control on the extent of particle fallout (Bursik et al., 1992; Sparks et al., 1992). The size of a particle controls its settling ve-

Table 4
Source Conditions Used for the Results Presented in This Work (a) ESPs for the General Simulations in Section 4.1, (b) ESPs for Simulations in Section 4.1.1, 4.1.2 and 4.2, (c) ESPs for the August 29, 2011 in Section 5, Mount Etna Case Study Monte Carlo Simulations, Where [1] Refers to (Parfitt, 1998) and [2] Refers to (Freret-Lorgeril et al., 2021)

ESP	Inner plume		Outer plume	Standard integral model
a)				
Total MFR (kg s^{-1})		10^3–10^7		10^3–10^7
Temperature (K)	1,200–1,500		900–1,200	900–1,200
Velocity (m s^{-1})	75–200		75–200	75–200
Gas mass fraction	0.01–0.03		0.03–0.05	0.03–0.05
ε		0–1		N/A
GSD	log-normal, median between −7 and −1		log-normal, median between inner median and 6	log-normal, median between inner median and 6
b)				
Total MFR (kg s^{-1})		10^5		10^5
Temperature (K)	1,500		1,200	1,200
Velocity (m s^{-1})	100		100	100
Gas mass fraction	0.01		0.03	0.03
ε		$\frac{2}{3}$		N/A
GSD	log-normal, median −7/−3		log-normal, median 0.5	log-normal, median 0.5
c)				
Total MFR (kg s^{-1})		$9 \times 10^3 - 10^6$		$9 \times 10^3 - 10^6$
Temperature (K)	1,200–1,500		900–1,200	900–1,200
Velocity (m s^{-1})	75–200		75–200	75–200
Gas mass fraction	0.01–0.03		0.03–0.05	0.03–0.05
ε		0.74		N/A
GSD	Hawaiian GSD[1]		Etna GSD[2]	Etna GSD[2]

locity, which in turn contributes to how much solid material falls out and if it is subsequently supported by the surrounding outer plume. Few studies exist of GSDs from field deposits of lava fountains (Andronico, Scollo, Cristaldi, & Lo Castro, 2014; Edwards et al., 2018; Parfitt, 1998). It is not possible to fully constrain this parameter in real time (Scollo et al., 2019). This results in the lava fountain GSD being poorly constrained and a large source of error.

To explore the sensitivity of the model to different GSDs, we vary the initial GSD of the lava fountain for four different sized hypothetical eruptions. The eruption sizes that we consider have initial MFRs of 10^3 kg s^{-1}, 10^4 kg s^{-1}, 10^5 kg s^{-1} and 10^6 kg s^{-1}. First, we determine the impact of a GSD composed of a single size on plume rise to clearly see the effect (Figure 6), and then with a log-normal GSD to better represent GSDs observed from real eruptions (Figure 7; Costa, Pioli, & Bonadonna, 2016; Pioli et al., 2019). All other ESPs are kept constant (velocity, temperature, gas mass fraction, ε) and are listed in Table 4b. The GSD of the outer plume is kept constant as a log-normal distribution with a median grain-size of 0.5 phi and a standard deviation of 1.5 phi, which is similar to the default value that is set to forecast tephra fallout in near real time (Scollo et al., 2019). This is also used as the initial GSD for the standard integral model. We compare results from a standard integral model to the double plume model for the two different coupling scenarios previously defined in Section 3.5.

For a lava fountain where the initial GSD consists of a single particle size, the final plume height is lower than that predicted by the standard integral model for lava fountain grain sizes coarser than approximately −6 phi (Figure 6). An initial coarse single-size GSD leads to significant fallout from the inner plume. Large particles that have fallen out are not supported by the outer plume and are, therefore, completely removed from the system when they fall from the lava fountain. The associated loss of mass, momentum and enthalpy from this process

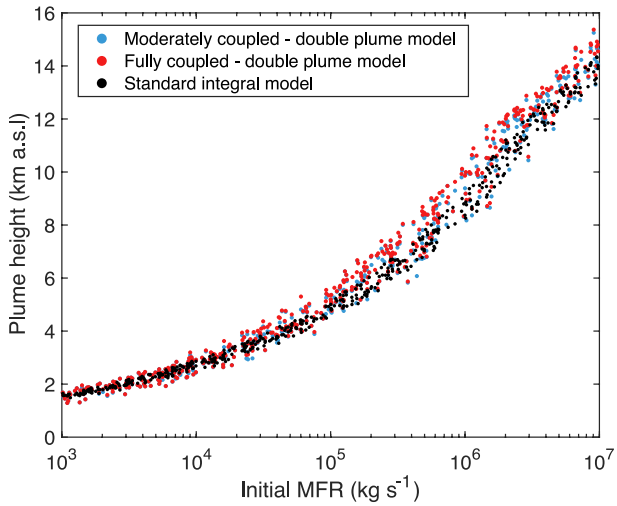

Figure 5. A comparison of the maximum height that plumes with different initial MFRs can reach between a standard integral (black markers) and a double plume model (colored markers). Two different coupling scenarios of the double plume model are presented; red markers refer to when the MFR is included in the start of the single plume region depending on the velocity (fully coupled) and blue markers where any MFR at the top of the lava fountain is completely removed (moderately coupled; see Section 3.5 for more details). MFR, mass flow rate.

results in the plume not reaching the same heights as the standard integral model despite having a hotter inner core. As the initial single-size GSD of the inner plume becomes finer, less fallout occurs leaving more mass, momentum and enthalpy in the whole plume system for it to go higher. The inner plume loses the majority of its solid phase MFR by the time the velocity reaches approximately 0 m s^{-1}. As a result, there is nothing left in the inner plume once it has stopped to add to the start of the single plume region. The different coupling schemes (solid blue and dashed red lines, Figure 6) thus become unimportant.

For the case when the lava fountain is composed of a single-size GSD between −6 and −4 phi (depending on the eruption size), with moderate coupling between the lava fountain and tephra plume, the final height of the plume decreases as the GSD becomes finer (solid blue line, Figure 6). As the GSD becomes finer, less fallout from the inner plume occurs. This results in the amount of MFR left in the inner plume, once the inner plume has stopped, increasing as the single-size GSD becomes finer. If this MFR is not added to the start of the single plume region, it is lost from the system. As a result, the initial mass, momentum and enthalpy of the single plume region is reduced. In the case of full coupling between the inner and outer plume (dashed red line, Figure 6), the final plume height remains constant, or decreases slightly, depending on the eruption size. This is because the majority of the mass, and related enthalpy and momentum is added to the start of the single plume region. As a result, the overall mass, enthalpy and momentum flow rates in the whole system is close to constant, so the final height of the plume does not significantly change.

The same behavior is observed when a log-normal GSD is used, rather than a GSD composed of only one grain-size, for the inner plume. The median of the log-normal GSD of the inner plume is varied between −7 and −2 phi and the standard deviation is kept constant at 0.75 phi (red lines, Figure 7b). We keep the inner plume GSD narrow to agree with observations of ultra-proximal deposits from Hawaiian lava fountains (Parfitt, 1998). When the lava fountain GSD is coarse, the double plume final height is lower than predicted by the standard integral model. As the GSD becomes finer, less material is lost from the system due to lower fallout occurring. This allows the plume to rise higher until the GSD becomes so fine that material that falls out of the inner plume is supported by the outer plume. At this point the coupling mechanism at the top of the plume becomes important. If any material left in the inner plume once it has stopped is not added to the source of the single plume region (moderately coupled), the single plume region starts with the same mass, momentum and enthalpy as the top of the outer plume. The inner plume mass, momentum and enthalpy flow rates at the point where it stops is lost from the system and the final height of the plume decreases as the GSD becomes finer. On the other hand, if the material of the inner plume is added and can be supported at the top of the double plume region (dashed red line, Figure 7) the overall plume height does not significantly vary as the median of the grain-size decreases. The overall mass, momentum and enthalpy flow rates of the system is generally conserved. The behavior of the plume from varying the GSD is the same for eruptions of different sizes as defined by the initial MFR.

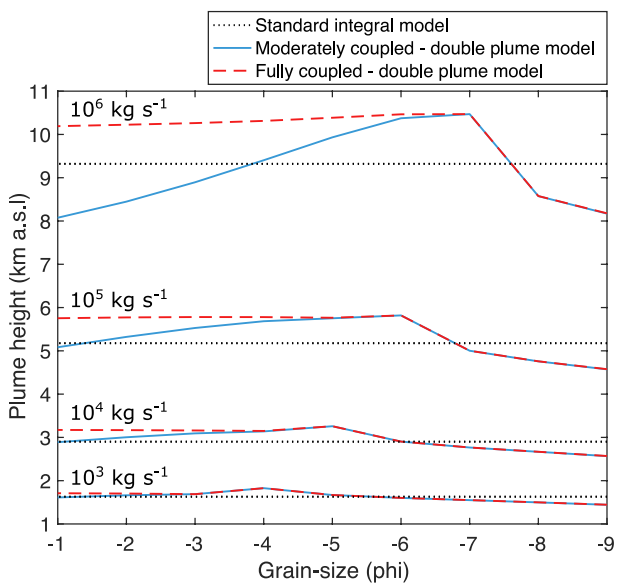

Figure 6. The effect of varying the single-size GSD of the inner plume on the overall plume height for four initial MFRs. For each MFR, the results of the standard integral model (black line) and the two scenarios of the double plume model, listed in Section 3.5, (dashed red and solid blue, respectively) are shown. MFR, mass flow rate.

4.1.2. Impact of Lava Fountain Size on Plume Rise

To vary the size of the lava fountain in the model, the partition ratio, (ε), is varied between 0.25 and 0.9. The bigger ε, the more of the initial MFR

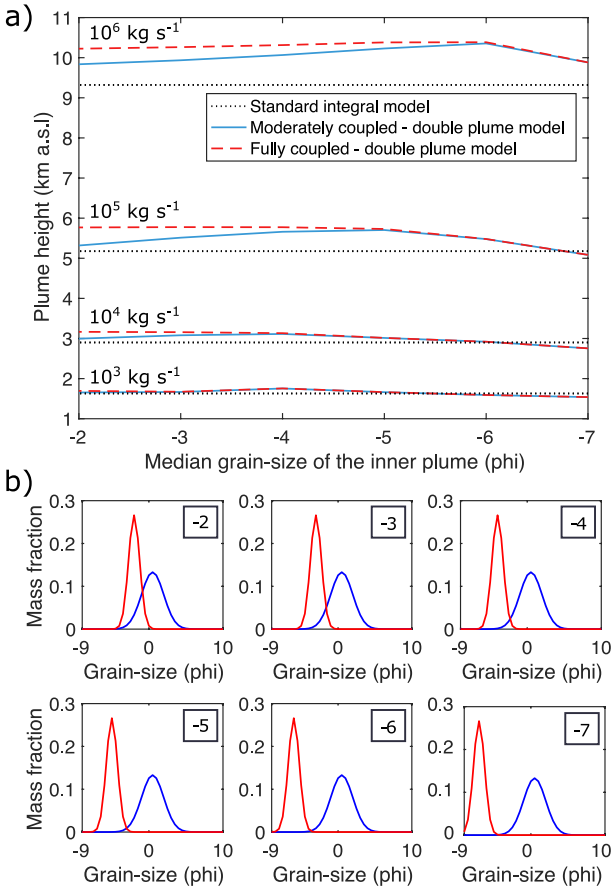

Figure 7. (a) The effect of varying the median size of the GSD of the inner plume on the overall plume height for the four initial MFRs investigated. For each MFR, the results from the standard integral model (black line) and the two scenarios of the double plume model, that are listed in Section 3.5, (dashed red and solid blue, respectively) are shown. (b) The GSDs of the inner (red) and the outer (blue) plume. The median size of the inner plume GSD, which correlates to the *x*-axis in (a), is referenced in the top right corner of each plot. MFR, mass flow rate.

partitioned into the inner plume, thus forming a larger lava fountain. The other source conditions (velocity, temperature, gas mass fraction, and GSD) are kept constant and can be found in Table 4b. We examine the effect of different sizes of lava fountains on the two coupling scenarios, moderately and fully coupled (Section 3.5).

An increase in the size of a lava fountain, when the inner plume has a log-normal GSD with a median of −3 phi, results in the tephra plume rising higher compared to when the lava fountain is small and to a standard volcanic plume. This is true for both the moderately and fully coupled scenarios (Figure 8a, solid blue and dashed red lines, respectively). As the lava fountain increases in size, the amount of fallout from the inner plume becomes proportionally larger compared to what is in the outer plume. When the fallout is composed of predominately finer particles (Figure 8a), the sedimenting particles become a source of mass, momentum and enthalpy for the outer plume. With larger lava fountains, this contribution of the hot material becomes the dominant component of the solid phase MFR in the outer plume rather than the original solid phase MFR erupted at the vent. The mass, momentum and enthalpy of the outer plume increases considerably resulting in a higher buoyant plume compared to if a lava fountain was not present.

In contrast, when the initial GSD of the inner plume is coarser (log-normal GSD with a median of −7 phi, we find a dependence on the initial MFR. For initial MFRs 10^5 kg s^{-1} or below, an increase in the size of a lava fountain results in the plume rising to lower heights with respect to the standard integral model. If the lava fountain consists of predominately large particles, much of the fallout from the inner plume is not supported by the surrounding plume. The sedimenting particles from the lava fountain are lost from the system, therefore the associated mass, momentum and enthalpy are also lost. The lower levels of mass, momentum and enthalpy being added to the outer plume results in the plume being unable to rise to heights similar to or greater than the standard integral model (Figure 8b). The two different coupling approaches are the same as large amounts of fallout results in the majority of the solid phase MFR of the inner plume being lost before the inner plume velocity approaches 0. Little or nothing is present to add to the start of the single plume region, and therefore the coupling mechanism becomes unimportant. However, when the initial GSD of the inner plume is coarse and the initial MFR is high (i.e., 10^6 kg s^{-1}), we see the same behavior as we did when the GSD of the inner plume was finer. Plume height increases as the lava fountain size increases because the overall larger initial MFR of the eruption results in the velocity profile of the outer plume decreasing at a slower rate with height compared to an eruption with a lower initial MFR. As a result, more of the fallout from the inner plume can be supported by the outer plume and the lava fountain acts as a source of mass and energy. As the lava fountain size increases, this source to the outer plume increases and therefore the plume can reach greater heights. This supports the results of a coupled plume going higher than a standard plume at high initial MFRs as seen in Figure 5.

4.2. Characteristics of a Coupled Lava Fountain–Tephra Plume

The inclusion of a lava fountain affects not only the rise height of the plume, but also its dynamics. Figures 9 and 10 show the velocity, temperature, radius, and density profiles for the double and single plume region, respectively. We compare two cases: when the GSD of the inner plume is coarse (Figures 9b and 10b) and when the GSD is fine (Figures 9a and 10a). Coarse and fine refer to log-normal distributions where the median grain-sizes are −7 and −3 phi, respectively. The standard deviation is kept constant at 0.75 phi. The other source conditions are kept constant and are shown in Table 4b. The initial MFR was set to 10^5 kg s^{-1} and 2/3 of this MFR is partitioned into the inner plume. Both the coupling scenarios of the double plume model and the standard integral

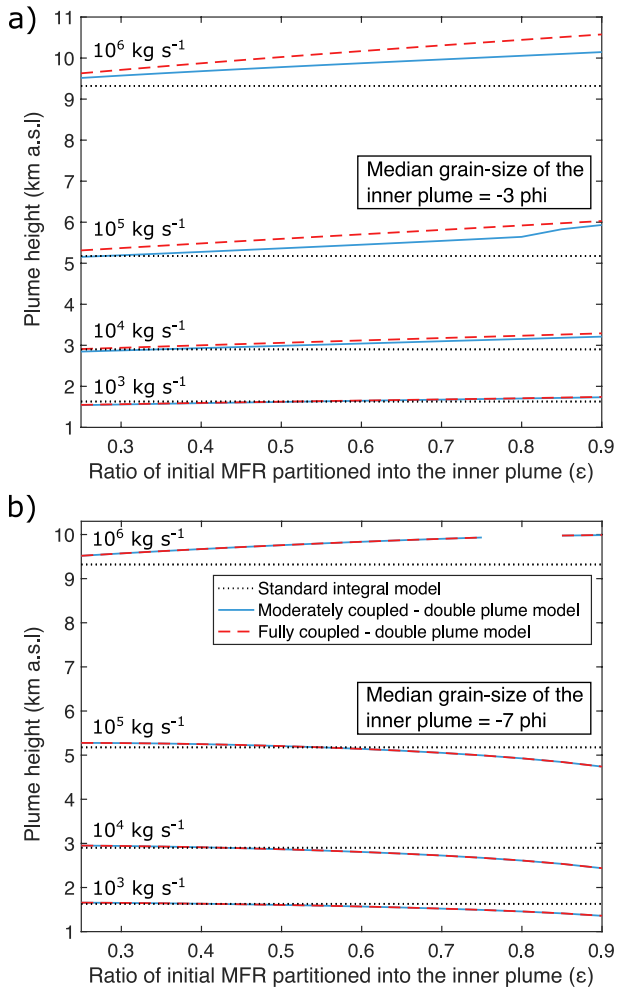

Figure 8. The effect of lava fountain size on the height of the coupled tephra plume (colored lines) compared to those of a standard integral model (black dotted line) for four different eruption; (a) shows the example of when the inner plume is initiated with a fine GSD, (b) shows the example of when the inner plume is initiated with a coarse GSD.

model are plotted. As both scenarios only differ in the treatment of the initial conditions of the single plume, both scenarios are the same for the double plume region. Reference to the dynamics of the inner and outer plumes in Figure 9 refers to both scenarios. We consider representative characteristics for two end-member scenarios and therefore cover the range of plausible outcomes.

4.2.1. The Height of the Double Plume Region

A key feature of the dynamics of the inner plume is that its height is much lower than that of a typical tephra plume. The height of the inner plume (i.e., the lava fountain) is controlled by its initial velocity and the extent of particle fallout. As the lava fountain never becomes buoyant, the maximum height it can reach is the ballistic height. If the inner plume loses the majority of its mass as it rises via the process of particle fallout, the solid phase MFR becomes negligible, and the lava fountain never reaches the ballistic height. When the GSD of the inner plume is fine, the inner plume height is comparable to the ballistic height (Figure 9a). The height of the inner plume is 516 m, while the height of the calculated ballistic height is 510 m for the source conditions defined in Table 4b. These heights are not comparable to the height of the gas thrust region (6–8 m) of the surrounding tephra plume or to the height of the gas-thrust region in a tephra plume without a lava fountain (25 m). However, when the GSD is coarse, the inner plume stops rising before the ballistic height is reached as the solid material in the plume is depleted (Figure 9b). Therefore, the dominant controls on the height of the inner plume (i.e., the lava fountain) differ to those of the surrounding plume, which in turn results in different dynamics between the inner and outer plume.

4.2.2. The Dynamics of the Double Plume Region

The dynamics of a lava fountain differs to those of the surrounding tephra plume (Figure 9) as, unlike the outer plume, the inner plume does not entrain the surrounding gas. The inner plume does not become buoyant as its density is always higher than that of the surrounding plume; it is a negatively-buoyant plume. The decrease of MFR due to the lack of entrainment into the inner plume and particle fallout results in the radius of the inner plume to decrease with height, while the velocity of the inner plume continuously decreases as it rises. The lack of entrainment of colder gas also causes very little cooling of the inner plume. In contrast the outer plume cools significantly and increases in width as it entrains the colder ambient gas. Once enough gas has been entrained and heated, the buoyancy is reversed causing an increase in the velocity of the outer plume. These characteristics of the outer plume are comparable to those of the standard integral model, with a slight difference due to the different entrainment coefficients used in the respective models.

The amount of sedimentation from the inner plume also plays a role in the dynamics of the inner plume and of the surrounding outer plume. When fallout is low (Figure 9a), the inner plume stops due to its velocity approaching 0 m s^{-1}, which causes the plume radius to diverge. The gas phase in the inner plume is depleted before all the solid mass has fallen out of it, causing the bulk plume density to tend toward that of the solid phase. However, when fallout is high (Figure 9b), the plume stops before the plume radius diverges as the solid material in the plume has completely fallen out. Initially, before significant amount of entrainment occurs into the outer plume, high fallout from the inner to the outer plume causes the temperature of the surrounding tephra plume to increase. The gas phase becomes the dominant phase of the inner plume, and therefore reduces the bulk density of the inner plume toward that of the gas phase. At the very top of the inner plume, the bulk density appears to increase. This is an artifact caused by the model as the radius of the inner plume becomes narrower than the diameter of the smallest grain-size present in the inner plume. The choice of the initial GSD can result in significant difference in the dynamics of the inner plume and influences the dynamics of the surrounding tephra plume.

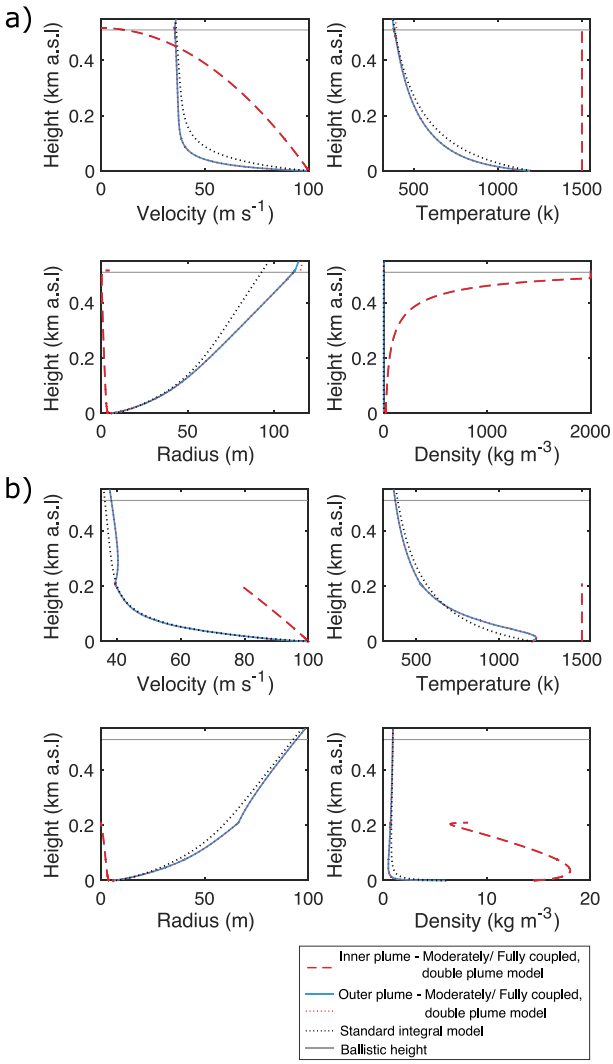

Figure 9. The dynamics (velocity, temperature, radius, and density) of the inner and outer plume (with the moderately and fully coupled scenarios overlapping) in the double plume region compared to those of the standard integral model. (a) The example of when the inner plume is initiated with a fine GSD and (b) is the case when the inner plume is initiated with a coarse GSD. The standard integral model is shown (dotted black line) for comparison and the modeled surrounding plume in the double plume is also plotted for completeness.

4.2.3. The Dynamics of the Single Plume Region

In the single plume region, there is little difference in dynamics between a tephra plume coupled to a lava fountain, for either coupling scenario, and a standard tephra plume (Figure 10), with the largest difference seen most strongly just above the lava fountain. There, the velocity of the plume increases before decreasing again. This is because the rate at which momentum in the plume increases is greater than that of the MFR. The radius, temperature and density of the single plume region follow the same general behavior as the plume without a lava fountain. The radius of the single plume starts wider, before becoming narrower with height, compared to the standard integral model. The density of the outer plume is lower than that of the standard modeled plume.

The small differences in the dynamics of the single plume region in the doule plume model, compared to the standard integral model, depend on the coupling scenario and how much material is left in the inner plume once it has stopped. When the initial GSD of the inner plume is coarse (Figure 10b), high sedimentation results in the single tephra plume being slightly colder, denser and wider as it rises compared to the standard integral model. No difference exists between the moderately and fully coupled double plume scenarios (solid dark blue vs. dotted red lines, Figure 10a) as nothing is left at the top of the inner plume to add to the start of the single plume. In contrast, when the initial inner plume GSD has a median grain-size of −3 phi (Figure 10a), the difference between the double plume model and the standard integral model is more significant; especially toward the top of the plume as it rises higher. In the case where the double plume and single plume region are fully coupled, the single plume starts off with higher mass, momentum and enthalpy flow rates as the majority of the material left at the top of the inner plume is added to the start of the single plume. This results in a discontinuity in the transition of the outer plume to the single plume. The single plume is slightly hotter and less dense than that of the plume without a lava fountain and a surrounding tephra plume that is moderately coupled to a lava fountain.

5. Case Study: The August 29, 2011 Paroxysm of Mount Etna, Italy

To understand the dynamics and the source conditions of volcanic plumes coupled with lava fountains, we apply the investigated integral plume models (double and standard) to the August 29, 2011 eruption of Mount Etna. This eruption produced a transitional (Scollo et al., 2019) ash-rich plume that reached a maximum height of 9.6 ± 0.3 km a.s.l (Corradini et al., 2018) and a mean height of 9 km a.s.l (Freret-Lorgeril et al., 2021). Thermal cameras recorded a thermally-saturated region above the vent with an average and maximum height of 453 and 1,080 m a.v.l, respectively (Calvari et al., 2018). The climactic phase of the eruption began at 03:50 GMT and lasted for 63 min (Freret-Lorgeril et al., 2018). Analysis of the field deposit determined a MFR of 3–4 × 10^4 kg s^{-1} (Freret-Lorgeril et al., 2021), and will hence be referred to as the plume tephra deposit MFR. The most proximal sample site of this field analysis was located 0.7 km from the vent. The GSD has been determined from analysis of the plume tephra deposit based on two different approaches, that is, based on observed data only or on a combination of observed and synthetic data (Figure 11; Freret-Lorgeril et al., 2021). The specific plume dynamics, and the availability of the observations, results in this eruption being an ideal example to analyze with the double plume model.

We take a Monte Carlo approach to invert the initial MFR of the August 29, 2011 eruption of Mount Etna using the double plume and standard integral model. Observations of both the plume and lava fountain heights are

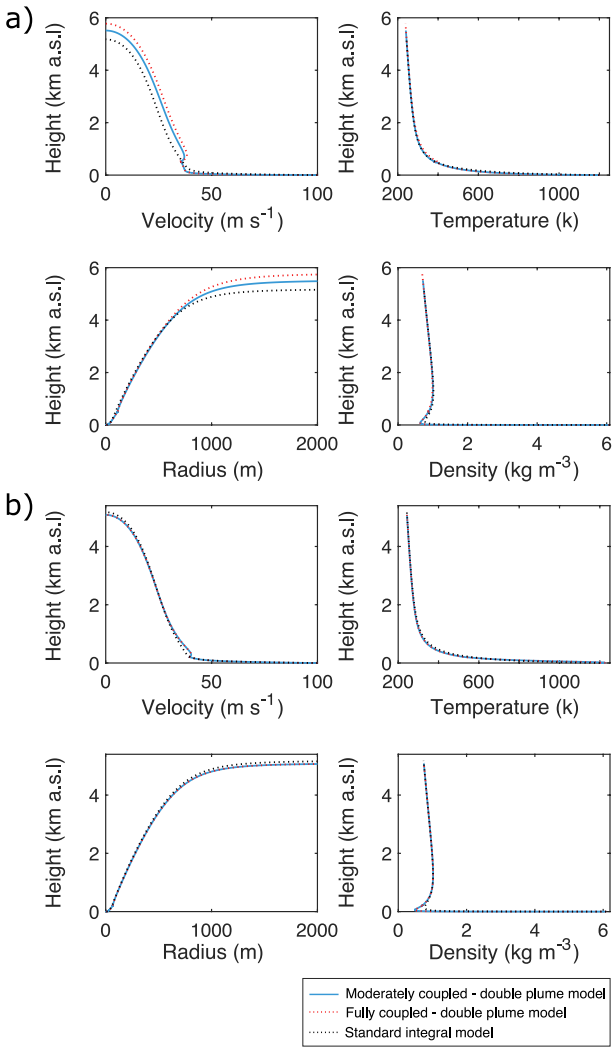

Figure 10. The dynamics (velocity, temperature, radius, and density) of the surrounding tephra plume for two examples, where one has a fine and the other has a coarse initial GSD for the inner plume, (a) and (b), respectively). The two different coupling scenarios are shown; solid blue line for the moderately coupled case and dotted red line for the fully coupled case. The standard integral model is shown (dotted black line) for comparison.

used to constrain the new double plume model, whereas the standard integral model can only be constrained by the plume height. By varying the selected ESPs (velocity, temperature, gas mass fraction, and MFR) of the plume models and comparing the modeled lava fountain and/or plume-top heights with observations, we can invert for the initial MFR. The observed lava fountain height is taken to be that of the saturated region in thermal camera images (Calvari et al., 2018). If the determined heights of the double plume region and the overall plume lie between the reported mean and maximum heights (Corradini et al., 2018; Calvari et al., 2018; Freret-Lorgeril et al., 2021) of the lava fountain and tephra plume, respectively, the simulation is recorded as a match. This procedure allows the range of initial MFRs that resulted in the observed plume and lava fountain heights to be determined.

The range of source conditions for the Monte Carlo simulations to determine the MFR range for the August 29, 2011 Mount Etna eruption are reported in Table 4c. For the double plume model, the inner plume is always hotter and contains a lower fraction of initial gas to represent a lava fountain. The partition ratio (ε) is kept constant at 0.74. This value is determined by the ratio between the estimated MFR of the cone deposit and the MFR of the cone deposit plus the MFR of the plume tephra deposit for the August 29, 2011 paroxysmal eruption of Mount Etna. The value of the MFR of the plume tephra deposit is reported in Freret-Lorgeril et al. (2021). The MFR of the cone deposit is calculated by taking the reported cone volume and total lava fountaining duration between 2011 and 2012 from Behncke et al. (2014), and assuming a density of the cone deposit of 1,800 kg m^{-3} (Mulas et al., 2016). Both the inner and outer plumes start with the same initial velocities. The standard integral model uses the same initial temperature, gas mass fraction and velocity as the outer plume. For each run, the atmospheric temperature and pressure profiles are taken from the ECMWF ERA Interim, Daily data sets for the location of Mount Etna on the August 29, 2011. The partition ratio (ε) and initial GSDs are also kept constant.

We use two different GSDs, as determined by Freret-Lorgeril et al. (2021) from the plume tephra deposit of the August 29, 2011 Mount Etna eruption, as the initial GSD of the outer plume. These two GSDs refer to a GSD only based on deposit sampling and a GSD based on a combination of deposit sampling and synthetic data used to fill the gap between field samples. Each GSD is used to initialize a simulation. We use the two reported GSDs to investigate the sensitivity of the plume rise to GSD calculation by different approaches; where all the samples are used to create the GSD and where synthetic data are also used. We assume that the wider field-based GSD is only representative of the outer plume as it does not contain any data from the proximal cone deposit as the most proximal sample (~700 m from the vent) lies out of the circumference of the cone as outlined by Behncke et al. (2014). The cone deposit is thought to be predominately composed of the tephra that has fallen out from the lava fountain (Behncke et al., 2014; Head & Wilson, 1989). As no GSDs exist from the cone deposit of Mount Etna, we use the GSD from the 1956 Kilauea Iki, Hawaii eruption (Figure 11), which does include an estimation of the most proximal cone deposit (Parfitt, 1998). The 1956 Kilauea Iki, Hawaii eruption was a coupled lava fountain–tephra plume, but the tephra plume was not of the same scale of those observed at Mount Etna, Italy as the plume height was much lower (Parfitt & Wilson, 1999). To initiate the standard integral model, we use the GSD derived from the plume tephra deposit as we do for the outer plume. This is because the standard integral model is modeling a tephra plume rather than a tephra plume and a lava fountain; therefore the initial GSD should only reflect the material in the plume tephra deposit. All the initial GSDs used in the modeling are plotted in Figure 11 and range from −9.5 phi to 4.5 phi with a spacing of 0.5 phi. Results of the MFR at different heights in the plume for each of the Monte Carlo simulations are shown on Figure 12.

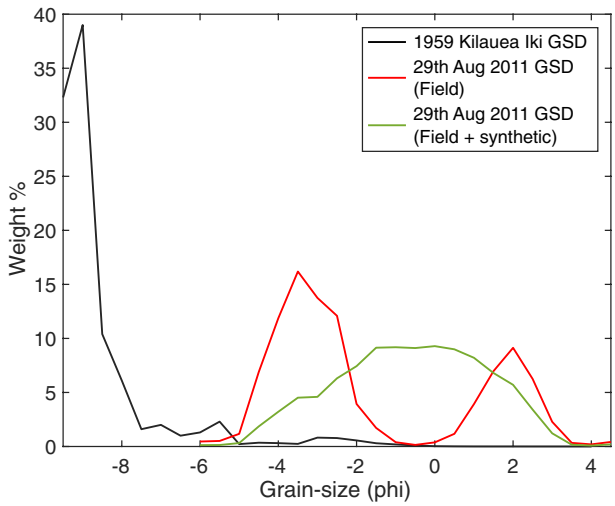

Figure 11. The initial GSDs used to model the August 29, 2011 eruption at Mount Etna, Italy. The inner plume initial GSD (black line) is kept constant, while the initial outer plume GSD (colored lines) is varied for each of the two Monte Carlo simulations.

The double plume model, regardless of the GSD used to initiate the outer plume, requires a slightly higher initial MFR to reach the same height as the standard integral model (Figure 12). This is because the inner plume is initiated with a coarse GSD (black line–Figure 11). In the cases where the initial GSD of the inner plume is coarse that is, as in a lava fountain, much of the fallout from the inner plume is not supported by the outer plume and is subsequently removed from the system. This results in the plume reaching lower heights than the standard integral model despite starting with overall more enthalpy within the inner plume as fallout removes much of the available enthalpy completely from the system.

Despite these differences in the initial MFR determined from the double and standard integral model, neither correspond with the MFR from the plume tephra deposit for the August 29, 2011 eruption. Figure 12 shows that the modeled MFRs at source (black and colored dots) are an order of magnitude higher than those determined from the plume tephra deposit and eruption duration (orange line). This is a feature that is often observed with coupled lava fountain-tephra plumes at Mount Etna, Italy (Figure 3). The double plume model does not reach the observed height of the tephra plume produced by the August 29, 2011 eruption with the MFR from the plume tephra deposit. This suggests that the additional heat from the hotter inner core (the lava fountain) does not result in the tephra plume going higher for a given MFR compared to a plume that does not have a lava fountain. The modeled MFR of the source, for the double plume model, best fits the sum of the MFR from the cone deposit and the MFR from the plume tephra deposit. This suggests that a considerable amount of the erupted material for this eruption is deposited in the proximal cone deposit.

While the plume tephra deposit MFR does not correspond to the MFR at the source of the plume, it does match with modeled MFRs just above the top of the lava fountain in the double plume model. Figure 12 highlights that the plume tephra deposit MFR (orange line) overlaps with the MFRs from the start of the single plume (colored open circles). As there is not a source of solid MFR in the system, the overall solid MFR in the double plume can only remain constant or decrease with plume rise. Significant levels of fallout occur of coarse material in the region where a lava fountain is present. This causes the solid MFR to decrease drastically in this zone to a value that is comparable to the MFR determined by the field deposit analysis.

6. Discussion

6.1. What Controls the Effect That a Lava Fountain has on Buoyant Plume Rise?

The extent to which a lava fountain affects the rise of a buoyant tephra plume depends on the amount of coupling between the tephra plume and the lava fountain. The greater the degree of coupling, the greater amounts of mass, momentum and enthalpy the lava fountain can provide to the rising tephra plume. This can result in the surrounding tephra plume reaching higher altitudes compared to those without these additional sources. Instances of high coupling include when fallout from the lava fountain is high, and this fallout is incorporated into surrounding plume or is transferred to the single plume region when the lava fountain stops. High fallout generally occurs when the initial GSD is coarse. The larger the solid particles in the plume, the more likely the velocity of the inner plume will not be high enough to support their rise and will subsequently sediment from the plume (Figures 6 and 7). If there is not any coupling between the lava fountain and the tephra plume, the lava fountain acts as a sink for the system. This occurs when the amount of fallout is really high, and the material is not supported by the surrounding plume, or when the fallout is low and the material is removed from the system when the lava fountain stops. These results lead to the conclusion that the initial GSD of a lava fountain is one of the most important controls on the extent of impact a lava fountain has on the rise of the surrounding tephra plume. Regardless of the type of coupling scenario, the effect on plume rise is greater when more of the overall initial MFR is partitioned into the lava fountain compared to the surrounding tephra plume (Figure 8).

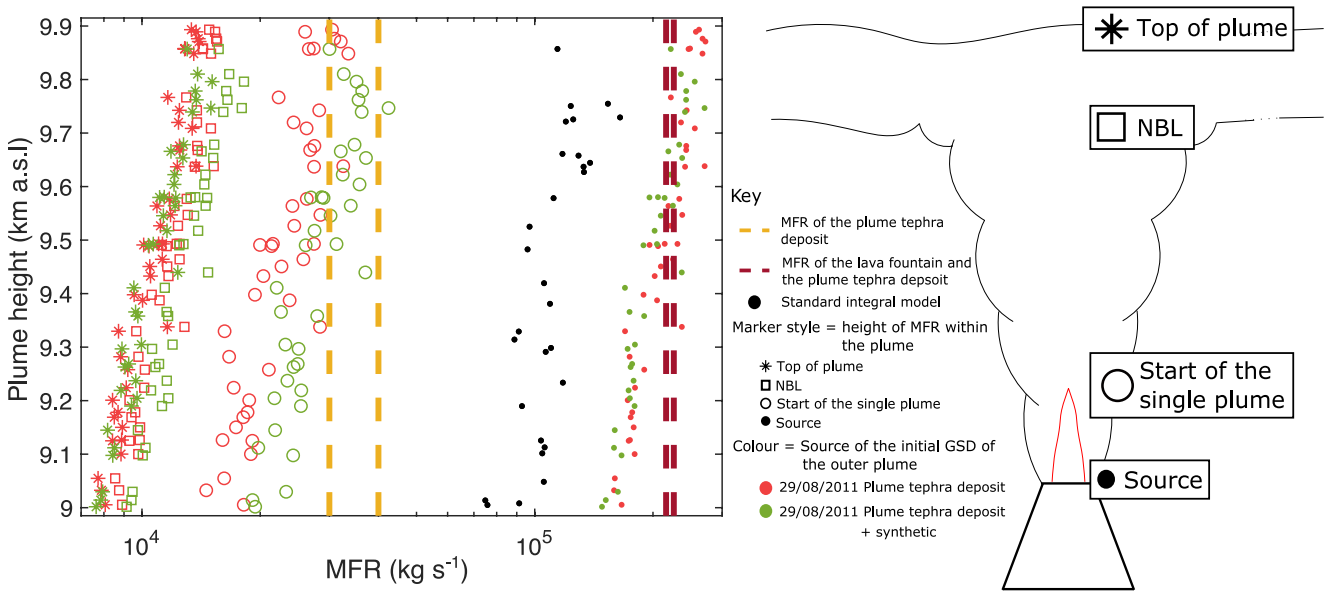

Figure 12. The modeled MFRs from the different Monte Carlo simulations when the model is constrained by the observations of the August 29, 2011 eruption of Mount Etna. The range of MFRs determined from the plume tephra deposit is marked with the orange dashed lines (Freret-Lorgeril et al., 2021). The burgundy lines refer to the MFR from the cone deposit plus from the MFR of plume tephra deposit; that is, an estimation of the total MFR of the explosive material from the eruption. Black markers refer to constrained model runs from the standard integral model and colored markers to model runs of the double plume model matched to the observations. The different colors of the markers refer to the initial GSD used for the outer plume in the double plume model. Red refers to the GSD used for the outer plume, where only the sampled points are used to create the GSD, and the green markers refer to a GSD where synthetic data is used to compensate for the lack of medial data to create the GSD. The different marker shapes refer to the location in the plume of the MFR; solid dots refer to the source, open circles to the start of the single plume just above the lava fountain, squares to the neutral buoyancy level (NBL) and stars to the top of the single plume. A schematic of the plume, that shows the different locations of the MFR values in the plume, is shown on the right-hand side of the figure.

6.2. What is the Relation Between Tephra Deposits and Coupled Lava Fountain–Tephra Plumes?

The MFR at the vent of a tephra plume coupled to a lava fountain, when determined from the numerical modeling, is different from the MFR calculated from the plume tephra deposit. For the case study explored in Section 5, the modeled MFR at the vent, from the double and standard integral models, are an order of magnitude larger than the MFR determined from analysis of the plume tephra deposit. The same pattern is seen with multiple other eruptions at Mount Etna, Italy (Figure 3). However, as Figure 12 highlights, the plume tephra deposit MFR for the August 29, 2011 eruption better correlates with modeled values of the MFR at the start of the single plume just above the lava fountain (Figure 12). This indicates that the plume produced a significant fallout in the proximal region.

Considering the differences between the MFR at the source and the MFR derived from the plume tephra deposit, an important question to ask is which MFR should be used to determine subsequent dispersion of the tephra in the atmosphere. MFR is a key input of volcanic dispersion models. However, significant uncertainty exists in determining its value for an eruption (e.g., Bonadonna et al., 2015). The MFR determined by a standard integral model overestimates the amount of ash that reaches the top of the plume and can be dispersed from the volcano. The same is true for the MFR at the source of the double plume model. It would be more suitable to use the solid MFR at the NBL, as determined from the double plume model, as a source term for further investigations into distal atmospheric dispersion, as this represents the erupted material that reaches the umbrella cloud. This value could be similar to the value derived from the plume tephra deposit but is different from the total initial MFR as determined from the standard integral model or from the combined cone and plume tephra deposit, which mainly depends on the spatial distribution of the tephra samples (Andronico, Scollo, Cristaldi, & Lo Castro, 2014). However, the MFR from the plume tephra deposit can also be an overestimation of what reaches the top of the plume (Figure 12). Therefore, while the new double plume model offers more insight into the MFR distribution in the tephra plume, in such cases, care is required on using MFRs from different heights in the plume to examine distal ash dispersion.

6.3. Limitations of the Model

6.3.1. Unaccounted-For Processes

We focused this study on the coupling of a lava fountain to the plume, but there are of course a series of additional processes that can further influence plume dynamics that were not directly accounted for. We discuss the most important ones and their potential impact here. Heat transfer processes such as thermal disequilibrium are not modeled. Thermal disequilibrium can exist at variable levels between particles larger than −2 phi and the gas phase (Woods & Bursik, 1991). For the GSD of the 1956 Kilauea Iki, Hawaii eruption, that is used as the initial GSD of the lava fountain for August 29, 2011 Mount Etna case study, this equates to ∼98% of the material in the field deposit. This could mean that the heat transfer between the lava fountain and the surrounding plume is overestimated. However, as the extent of thermal disequilibrium is dependent on grain-size and a large amount of the coarse particles are removed completely from the system by particle fallout from the lava fountain, the significance of the reduction in heat transfer is assumed to be limited. Another unaccounted process is secondary fragmentation within the lava fountain, which could result in additional material being added to the surrounding plume.

Wind could also play a vital role on the rise of plumes that contain a lava fountain. Increased entrainment and bending of the plume from wind can reduce the overall height a standard tephra plume can reach. Its effect has been accounted for in standard integral model and has been studied in detail (Bursik, 2001; Carazzo et al., 2014; Degruyter & Bonadonna, 2012, 2013; Girault et al., 2016; Woodhouse et al., 2013). While it is reasonable to expect a similar effect for the tephra plume above the lava fountain, the impact of wind on the region of the tephra plume that coexists with the lava fountain is less clear. An increase of entrained fluid from the atmosphere into the tephra plume could affect its ability to support sedimenting material from the inner plume. High wind could also increase the stability of the tephra plume as has been highlight in standard tephra plumes by Degruyter and Bonadonna (2013).

6.3.2. Parameter Uncertainty

Another consideration of this study should be the values of the entrainment coefficients used in the integral plume models. While there has been an extensive amount of research of which values to use in standard integral models (Aubry et al., 2017; Aubry & Jellinek, 2018; Devenish, Rooney, Webster, & Thomson, 2010; Suzuki & Koyaguchi, 2015), including using varying entrainment coefficients that are dependable on the Richardson number (Carazzo et al., 2008; Kaminski et al., 2005), considerable uncertainty on their values remains. Entrainment coefficients for double plumes have been determined from large eddy simulation of Boussinesq plumes (0.05, 0.8, and 0.01 for α, β, and λ, respectively; Devenish, Rooney, & Thomson, 2010). They have also been calculated from the fitting of theoretical modeling to experiments of Boussinesq fountains (0.085, 0.147, and 0.147 for α, β, and λ, respectively; Bloomfield & Kerr, 2000). The coefficients from these different studies differ to each other and therefore lead to a difference in plume dynamics (Devenish & Cerminara, 2018). The plume height modeled by a double plume model is sensitive to the values chosen for the entrainment coefficients (Li & Flynn, 2020; Li et al., 2018). Given the importance of the values of the entrainment coefficients, and the structure of a coupled lava fountain–tephra plume being different to experimental Boussinesq fountains (hotter, coarser, and co-flowing), further experiments and analysis of real eruptions are needed to better constrain their values.

Even though the source conditions are a major control on the extent of coupling between a lava fountain and a tephra plume, the characterization of the GSD and lava fountain size of a coupled lava fountain–tephra plume system are poorly constrained. Such source parameters are difficult to determine. Field analysis of the proximal deposit is challenging after an eruption due to the difficult accessibility and deposit correlation (Andronico, Scollo, Cristaldi, & Lo Castro, 2014; Behncke et al., 2014). Frequent eruptions at volcanoes such as Mount Etna, make it difficult to determine one eruption deposit from another in the very proximal region. As a result, analysis of the GSDs and of the erupted material has not been carried out on the very proximal deposits of fallout forming the scoria cone from the lava fountains that occurred between 2011 and 2016. Further information on the GSDs of the inner plume would provide a better description of the initial grain-size characteristics of the lava fountain and would improve the reconstruction of coupled lava fountain–tephra plumes. Field studies of proximal cones produced by coupled lava fountains - tephra plumes should be carried out to determine the GSD of the lava fountain. To better determine the amount of erupted mass of the lava fountain, remote sensing methods, such as radar, could also be used to define the MFR partition ratio ε between the lava fountain and the surrounding tephra plume

(Freret-Lorgeril et al., 2018). High accuracy Lidar surveys (Fornaciai et al., 2010; Scollo et al., 2012, 2015) and Unmanned Aerial Vehicles investigations (De Beni et al., 2019) after individual eruptions could also provide details on the characteristics and the volume of the cone deposits to better estimate the partition ratio of the initial MFR.

7. Conclusions

We have developed a novel model for buoyant tephra plumes associated with a lava fountain, which indicates that lava fountains do affect the characteristics of buoyant tephra plumes. Results show that the type and extent of the effect on a plume from a coupled lava fountain is predominantly dependent on the amount of the initial MFR that is partitioned into the lava fountain in relation to the surrounding tephra plume and the GSD of the lava fountain. The presence of a lava fountain increases the variability of the MFR-plume height relationship, compared to those without. When a greater fraction of the overall initial MFR is partitioned into the lava fountain and if the fountain is composed of coarse material, the lava fountain acts as a sink of mass, momentum and enthalpy of the overall plume system. In this scenario, a higher MFR at the source is required to reach the same height as a plume without a lava fountain.

Our investigations show that while the lava fountain is momentum driven, it cannot always be assumed to be at its maximum ballistic height due to particle fallout and entrainment processes. In contrast, the height of the gas-thrust region of a tephra plume is not equal to the ballistic height since the plume becomes buoyancy driven before the latter is reached. Care and further work are needed to determine if the lava fountain height can be used to determine the exit velocity of the surrounding buoyant tephra plume.

The discrepancy between the MFR determined from plume height and the MFR determined from the field deposit could be explained by the change in the solid MFR with height, that is captured by the new double plume model. For the August 29, 2011 Mount Etna eruption, the MFR derived from the plume tephra deposit does not equate to what is erupted at the vent, but to what is still in the plume above the lava fountain. When a lava fountain is composed of coarse material, a larger majority of the tephra falls out of the lava fountain and does not reach the top of the plume. This highlights the importance of characterizing the near vent deposit when determining MFRs from the tephra deposit to ensure that the total erupted volume is not underestimated (Andronico et al., 2015; Behncke et al., 2014; De Beni et al., 2015; Freret-Lorgeril et al., 2018; Spanu et al., 2016). Furthermore, MFRs determined from a standard integral model could overestimate the amount of tephra that is released in the atmosphere during paroxysmal eruptions. It is important to choose the right modeled MFR from the double plume model, and to consider what the tephra deposit represents, for further use in atmospheric dispersion models, as what is erupted at the vent is not always comparable to what is released in the atmosphere.

One crucial issue for further work is to constrain key controls to correctly determine the effect of the lava fountain on plume rise. Further field and remote sensing analysis of the proximal cone deposit is needed to improve the estimate of the initial GSD and the initial mass partitioning between the lava fountain and tephra plume. Inclusion of wind and thermal disequilibrium in the double plume model would allow the effect of these processes to be explored and will further improve the applicability of the model.

Data Availability Statement

Access to the model code used to generate the data in this manuscript can be downloaded from https://zenodo.org/badge/latestdoi/313691946.

Acknowledgments
ES is supported by a NERC GW4+ Doctoral Training Partnership studentship from the Natural Environment Research Council [NE/L002434/1] and is thankful for the support and additional funding from CASE partner, Istituto Nazionale di Geofisica e Vulcanologia, Osservatorio Etneo. This project has also received funding from the European Union's Horizon 2020 research and innovation program under grant agreement No 731070 (EUROVOLC). We would also like to thank two annoymous reviewers for their comments which help to improve the manuscript.

References

Alparone, S., Andronico, D., Lodato, L., & Sgroi, T. (2003). Relationship between tremor and volcanic activity during the Southeast Crater eruption on Mount Etna in early 2000. *Journal of Geophysical Research*, *108*(B5). https://doi.org/10.1029/2002jb001866

Andronico, D., Behncke, B., De Beni, E., Cristaldi, A., Scollo, S., Lopez, M., & Lo Castro, M. D. (2018). Magma budget from lava and tephra volumes erupted during the 25−26 October 2013 lava fountain at Mt Etna. *Frontiers in Earth Science*, *6*, 116. https://doi.org/10.3389/feart.2018.00116

Andronico, D., Scollo, S., Caruso, S., & Cristaldi, A. (2008). The 2002-03 Etna explosive activity: Tephra dispersal and features of the deposits. *Journal of Geophysical Research*, *113*(B4). https://doi.org/10.1029/2007jb005126

Andronico, D., Scollo, S., & Cristaldi, A. (2015). Unexpected hazards from tephra fallouts at Mt Etna: The 23 November 2013 lava fountain. *Journal of Volcanology and Geothermal Research*, *304*, 118–125. https://doi.org/10.1016/j.jvolgeores.2015.08.007

Andronico, D., Scollo, S., Cristaldi, A., & Ferrari, F. (2009). Monitoring ash emission episodes at Mt. Etna: The 16 November 2006 case study. *Journal of Volcanology and Geothermal Research*, *180*(2–4), 123–134. https://doi.org/10.1016/j.jvolgeores.2008.10.019

Andronico, D., Scollo, S., Cristaldi, A., & Lo Castro, M. D. (2014). Representativity of incompletely sampled fall deposits in estimating eruption source parameters: A test using the 12-13 January 2011 lava fountain deposit from Mt. Etna volcano, Italy. *Bulletin of Volcanology*, *76*(10), 861. https://doi.org/10.1007/s00445-014-0861-3

Andronico, D., Scollo, S., Lo Castro, M. D., Cristaldi, A., Lodato, L., & Taddeucci, J. (2014). Eruption dynamics and tephra dispersal from the 24 November 2006 paroxysm at South-East Crater, Mt Etna, Italy. *Journal of Volcanology and Geothermal Research*, *274*, 78–91. https://doi.org/10.1016/j.jvolgeores.2014.01.009

Andronico, D., Spinetti, C., Cristaldi, A., & Buongiorno, M. F. (2009). Observations of Mt. Etna volcanic ash plumes in 2006: An integrated approach from ground-based and polar satellite NOAA-AVHRR monitoring system. *Journal of Volcanology and Geothermal Research*, *180*(2–4), 135–147. https://doi.org/10.1016/j.jvolgeores.2008.11.013

Aubry, T. J., Carazzo, G., & Jellinek, A. M. (2017). Turbulent entrainment into volcanic plumes: New constraints from laboratory experiments on buoyant jets rising in a stratified crossflow. *Geophysical Research Letters*, *44*(20), 10198–10207. https://doi.org/10.1002/2017gl075069

Aubry, T. J., & Jellinek, A. M. (2018). New insights on entrainment and condensation in volcanic plumes: Constraints from independent observations of explosive eruptions and implications for assessing their impacts. *Earth and Planetary Science Letters*, *490*, 132–142. https://doi.org/10.1016/j.epsl.2018.03.028

Azzopardi, F., Ellul, R., Prestifilippo, M., Scollo, S., & Coltelli, M. (2013). The effect of Etna volcanic ash clouds on the Maltese Islands. *Journal of Volcanology and Geothermal Research*, *260*, 13–26. https://doi.org/10.1016/j.jvolgeores.2013.04.019

Barsotti, S., Andronico, D., Neri, A., Del Carlo, P., Baxter, P. J., Aspinall, W. P., & Hincks, T. (2010). Quantitative assessment of volcanic ash hazards for health and infrastructure at Mt. Etna (Italy) by numerical simulation. *Journal of Volcanology and Geothermal Research*, *192*(1–2), 85–96. https://doi.org/10.1016/j.jvolgeores.2010.02.011

Behncke, B., Branca, S., Corsaro, R. A., De Beni, E., Miraglia, L., & Proietti, C. (2014). The 2011-2012 summit activity of Mount Etna: Birth, growth and products of the new SE crater. *Journal of Volcanology and Geothermal Research*, *270*, 10–21. https://doi.org/10.1016/j.jvolgeores.2013.11.012

Bloomfield, L. J., & Kerr, R. C. (1998). Turbulent fountains in a stratified fluid. *Journal of Fluid Mechanics*, *358*, 335–356. https://doi.org/10.1017/s0022112097008252

Bloomfield, L. J., & Kerr, R. C. (2000). A theoretical model of a turbulent fountain. *Journal of Fluid Mechanics*, *424*, 197–216. https://doi.org/10.1017/s0022112000001907

Bonaccorso, A., Calvari, S., Linde, A., & Sacks, S. (2014). Eruptive processes leading to the most explosive lava fountain at Etna volcano: The 23 November 2013 episode. *Geophysical Research Letters*, *41*(14), 4912–4919. https://doi.org/10.1002/2014gl060623

Bonadonna, C., Biass, S., & Costa, A. (2015). Physical characterization of explosive volcanic eruptions based on tephra deposits: Propagation of uncertainties and sensitivity analysis. *Journal of Volcanology and Geothermal Research*, *296*, 80–100. https://doi.org/10.1016/j.jvolgeores.2015.03.009

Bonadonna, C., Ernst, G. G. J., & Sparks, R. S. J. (1998). Thickness variations and volume estimates of tephra fall deposits: The importance of particle Reynolds number. *Journal of Volcanology and Geothermal Research*, *81*(3–4), 173–187. https://doi.org/10.1016/s0377-0273(98)00007-9

Bonadonna, C., & Phillips, J. C. (2003). Sedimentation from strong volcanic plumes. *Journal of Geophysical Research*(*108*, (B7). https://doi.org/10.1029/2002JB002034

Bursik, M. (2001). Effect of wind on the rise height of volcanic plumes. *Geophysical Research Letters*, *28*(18), 3621–3624. https://doi.org/10.1029/2001gl013393

Bursik, M. I., Sparks, R. S. J., Gilbert, J. S., & Carey, S. N. (1992). Sedimentation of tephra by volcanic plumes: I. Theory and its comparison with a study of the Fogo A plinian deposit, Sao Miguel (Azores). *Bulletin of Volcanology*, *54*(4), 329–344. https://doi.org/10.1007/bf00301486

Calvari, S., Cannavò, F., Bonaccorso, A., Spampinato, L., & Pellegrino, A. G. (2018). Paroxysmal explosions, lava fountains and ash plumes at Etna Volcano: Eruptive processes and hazard implications. *Frontiers in Earth Science*, *6*(August), 107. https://doi.org/10.3389/feart.2018.00107

Calvari, S., Salerno, G. G., Spampinato, L., Gouhier, M., La Spina, A., Pecora, E., et al. (2011). An unloading foam model to constrain Etna's 11–13 January 2011 lava fountaining episode. *Journal of Geophysical Research*, *116*(B11). https://doi.org/10.1029/2011jb008407

Carazzo, G., Girault, F., Aubry, T., Bouquerel, H., & Kaminski, E. (2014). Laboratory experiments of forced plumes in a density-stratified crossflow and implications for volcanic plumes. *Geophysical Research Letters*, *41*(24), 8759–8766. https://doi.org/10.1002/2014gl061887

Carazzo, G., Kaminski, E., & Tait, S. (2008). On the rise of turbulent plumes: Quantitative effects of variable entrainment for submarine hydrothermal vents, terrestrial and extra terrestrial explosive volcanism. *Journal of Geophysical Research*, *113*(B9). https://doi.org/10.1029/2007jb005458

Carey, S., & Bursik, M. (2015). Volcanic plumes. In *The encyclopedia of volcanoes* (pp. 571–585). Elsevier. https://doi.org/10.1016/b978-0-12-385938-9.00032-8

Carey, S., & Sparks, R. S. J. (1986). Quantitative models of the fallout and dispersal of tephra from volcanic eruption columns. *Bulletin of Volcanology*, *48*(2), 109–125. https://doi.org/10.1007/bf01046546

Corradini, S., Guerrieri, L., Lombardo, V., Merucci, L., Musacchio, M., Prestifilippo, M., et al. (2018). Proximal monitoring of the 2011-2015 Etna lava fountains using MSG-SEVIRI data. *Geosciences*, *8*(4), 140. https://doi.org/10.3390/geosciences8040140

Corradini, S., Montopoli, M., Guerrieri, L., Ricci, M., Scollo, S., Merucci, L., et al. (2016). A multi-sensor approach for volcanic ash cloud retrieval and eruption characterization: The 23 November 2013 Etna Lava Fountain. *Remote Sensing*, *8*(1), 58. https://doi.org/10.3390/rs8010058

Costa, A., Pioli, L., & Bonadonna, C. (2016). Assessing tephra total grain-size distribution: Insights from field data analysis. *Earth and Planetary Science Letters*, *443*, 90–107. https://doi.org/10.1016/j.epsl.2016.02.040

Costa, A., Suzuki, Y. J., Cerminara, M., Devenish, B. J., Esposti Ongaro, T., Van Eaton, A. R., et al. (2016). Results of the eruptive column model inter-comparison study. *Journal of Volcanology and Geothermal Research*, *326*, 2–25. https://doi.org/10.1016/j.jvolgeores.2016.01.017

De Beni, E., Behncke, B., Branca, S., Nicolosi, I., Carluccio, R., D'Ajello Caracciolo, F., & Chiappini, M. (2015). The continuing story of Etna's New Southeast Crater (2012-2014): Evolution and volume calculations based on field surveys and aerophotogrammetry. *Journal of Volcanology and Geothermal Research*, *303*, 175–186. https://doi.org/10.1016/j.jvolgeores.2015.07.021

De Beni, E., Cantarero, M., & Messina, A. (2019). UAVs for volcano monitoring: A new approach applied on an active lava flow on Mt. Etna (Italy), during the 27 February–02 March 2017 eruption. *Journal of Volcanology and Geothermal Research*, *369*, 250–262. https://doi.org/10.1016/j.jvolgeores.2018.12.001

Dee, D. P., Uppala, S. M., Simmons, A. J., Berrisford, P., Poli, P., Kobayashi, S., et al. (2011). The ERA-Interim reanalysis: Configuration and performance of the data assimilation system. *Quarterly Journal of the Royal Meteorological Society*, *137*(656), 553–597. https://doi.org/10.1002/qj.828

Degruyter, W., & Bonadonna, C. (2012). Improving on mass flow rate estimates of volcanic eruptions. *Geophysical Research Letters*, *39*. https://doi.org/10.1029/2012gl052566

Degruyter, W., & Bonadonna, C. (2013). Impact of wind on the condition for column collapse of volcanic plumes. *Earth and Planetary Science Letters*, *377–378*, 218–226. https://doi.org/10.1016/j.epsl.2013.06.041

de Michele, M., Raucoules, D., Corradini, S., Merucci, L., Salerno, G., Sellitto, P., & Carboni, E. (2019). Volcanic cloud top height estimation using the plume elevation model procedure applied to orthorectified landsat 8 data. Test case: 26 October 2013 Mt. Etna eruption. *Remote Sensing*, *11*(7), 785. https://doi.org/10.3390/rs11070785

Devenish, B. J. (2013). Using simple plume models to refine the source mass flux of volcanic eruptions according to atmospheric conditions. *Journal of Volcanology and Geothermal Research*, *256*, 118–127. https://doi.org/10.1016/j.jvolgeores.2013.02.015

Devenish, B. J. (2016). Estimating the total mass emitted by the eruption of Eyjafjallajökull in 2010 using plume-rise models. *Journal of Volcanology and Geothermal Research*, *326*, 114–119. https://doi.org/10.1016/j.jvolgeores.2016.01.005

Devenish, B. J., & Cerminara, M. (2018). The transition from eruption column to umbrella cloud. *Journal of Geophysical Research: Solid Earth*, *123*(12), 10418–10430. https://doi.org/10.1029/2018JB015841

Devenish, B. J., Rooney, G. G., & Thomson, D. J. (2010). Large-eddy simulation of a buoyant plume in uniform and stably stratified environments. *Journal of Fluid Mechanics*, *652*, 75–103. https://doi.org/10.1017/s0022112010000017

Devenish, B. J., Rooney, G. G., Webster, H. N., & Thomson, D. J. (2010). The entrainment rate for buoyant plumes in a crossflow. *Boundary-Layer Meteorology*, *134*(3), 411–439. https://doi.org/10.1007/s10546-009-9464-5

Durig, T., Gudmundsson, M. T., Karmann, S., Zimanowski, B., Dellino, P., Rietze, M., & Buttner, R. (2015). Mass eruption rates in pulsating eruptions estimated from video analysis of the gas thrust-buoyancy transition-a case study of the 2010 eruption of Eyjafjallajokull, Iceland. *Earth Planets and Space*, *67*(1). https://doi.org/10.1186/s40623-015-0351-7

Edwards, M. J., Pioli, L., Andronico, D., Scollo, S., Ferrari, F., & Cristaldi, A. (2018). Shallow factors controlling the explosivity of basaltic magmas: The 17-25 May 2016 eruption of Etna Volcano (Italy). *Journal of Volcanology and Geothermal Research*, *357*, 425–436. https://doi.org/10.1016/j.jvolgeores.2018.05.015

Ernst, G. G. J., Sparks, R. S. J., Carey, S. N., & Bursik, M. I. (1996). Sedimentation from turbulent jets and plumes. *Journal of Geophysical Research*, *101*(B3), 5575–5589. https://doi.org/10.1029/95jb01900

Fornaciai, A., Behncke, B., Favalli, M., Neri, M., Tarquini, S., & Boschi, E. (2010). Detecting short-term evolution of Etnean scoria cones: A LIDAR-based approach. *Bulletin of Volcanology*, *72*(10), 1209–1222. https://doi.org/10.1007/s00445-010-0394-3

Freret-Lorgeril, V., Bonadonna, C., Corradini, S., Guerrieri, L., Lemus, J., Donnadieu, F., et al. (2021). Tephra characterization and multidisciplinary determination of Eruptive Source Parameters of a weak paroxysm at Mount Etna (Italy). *Journal of Volcanology and Geothermal Research*, 10743. https://doi.org/10.1016/j.jvolgeores.2021.107431

Freret-Lorgeril, V., Donnadieu, F., Scollo, S., Provost, A., Fréville, P., Guéhenneux, Y., et al. (2018). Mass eruption rates of tephra plumes during the 2011–2015 lava fountain paroxysms at Mt. Etna from doppler radar retrievals. *Frontiers in Earth Science*, *6*, 73. https://doi.org/10.3389/feart.2018.00073

Girault, F., Carazzo, G., Tait, S., Ferrucci, F., & Kaminski, É. (2014). The effect of total grain-size distribution on the dynamics of turbulent volcanic plumes. *Earth and Planetary Science Letters*, *394*, 124–134. https://doi.org/10.1016/j.epsl.2014.03.021

Girault, F., Carazzo, G., Tait, S., & Kaminski, E. (2016). Combined effects of total grain-size distribution and crosswind on the rise of eruptive volcanic columns. *Journal of Volcanology and Geothermal Research*, *326*, 103–113. https://doi.org/10.1016/j.jvolgeores.2015.11.007

Glaze, L. S., Self, S., Schmidt, A., & Hunter, S. J. (2017). Assessing eruption column height in ancient flood basalt eruptions. *Earth and Planetary Science Letters*, *457*, 263–270. https://doi.org/10.1016/j.epsl.2014.07.043

Gouhier, M., Eychenne, J., Azzaoui, N., Guillin, A., Deslandes, M., Poret, M., et al. (2019). Low efficiency of large volcanic eruptions in transporting very fine ash into the atmosphere. *Scientific Reports*, *9*(1), 1–12. https://doi.org/10.1038/s41598-019-38595-7

Head, J. W., & Wilson, L. (1989). Basaltic pyroclastic eruptions: Influence of gas-release patterns and volume fluxes on fountain structure, and the formation of cinder cones, spatter cones, rootless flows, lava ponds and lava flows. *Journal of Volcanology and Geothermal Research*, *37*(3-4), 261–271. https://doi.org/10.1016/0377-0273(89)90083-8

Horwell, C. J., Sargent, P., Andronico, D., Lo Castro, M. D., Tomatis, M., Hillman, S. E., et al. (2017). The iron-catalysed surface reactivity and health-pertinent physical characteristics of explosive volcanic ash from Mt. Etna, Italy. *Journal of Applied Volcanology*, *6*(1), 12. https://doi.org/10.1186/s13617-017-0063-8

Kaminski, E., Tait, S., & Carazzo, G. (2005). Turbulent entrainment in jets with arbitrary buoyancy. *Journal of Fluid Mechanics*, *526*, 361–376. https://doi.org/10.1017/s0022112004003209

Kaminski, E., Tait, S., Ferrucci, F., Martet, M., Hirn, B., & Husson, P. (2011). Estimation of ash injection in the atmosphere by basaltic volcanic plumes: The case of the Eyjafjallajokull 2010 eruption. *Journal of Geophysical Research*, *116*(B9). https://doi.org/10.1029/2011jb008297

Li, S., & Flynn, M. R. (2020). Coaxial plumes in a windy ambient with applications to cooling towers. *Journal of Wind Engineering and Industrial Aerodynamics*, *196*, 104054. 104054. https://doi.org/10.1016/j.jweia.2019.104054

Li, S., Moradi, A., Vickers, B., & Flynn, M. R. (2018). Cooling tower plume abatement using a coaxial plume structure. *International Journal of Heat and Mass Transfer*, *120*, 178–193. https://doi.org/10.1016/j.ijheatmasstransfer.2017.12.040

Mannen, K. (2006). Total grain size distribution of a mafic subplinian tephra, TB-2, from the 1986 Izu-Oshima eruption, Japan: An estimation based on a theoretical model of tephra dispersal. *Journal of Volcanology and Geothermal Research*, *155*(1–2), 1–17. https://doi.org/10.1016/j.jvolgeores.2006.02.004

Mastin, L. G. (2014). Testing the accuracy of a 1-D volcanic plume model in estimating mass eruption rate. *Journal of Geophysical Research: Atmospheres*, *119*(5), 2474–2495. https://doi.org/10.1002/2013jd020604

Mastin, L. G., Guffanti, M., Servranckx, R., Webley, P., Barsotti, S., Dean, K., et al. (2009). A multidisciplinary effort to assign realistic source parameters to models of volcanic ash-cloud transport and dispersion during eruptions. *Journal of Volcanology and Geothermal Research*, *186*(1–2), 10–21. https://doi.org/10.1016/j.jvolgeores.2009.01.008

Mcdougall, T. J. (1978). Bubble plumes in stratified environments. *Journal of Fluid Mechanics*, *85*(4), 655–672. https://doi.org/10.1017/s0022112078000841

Mcdougall, T. J. (1981). Negatively buoyant vertical jets. *Tellus*, *33*(3), 313–320. https://doi.org/10.3402/tellusa.v33i3.10718

Mereu, L., Scollo, S., Bonadonna, C., Freret-Lorgeril, V., & Marzano, F. S. (2020). Multisensor Characterization of the Incandescent Jet Region of Lava Fountain-Fed Tephra Plumes. *Remote Sensing*, (Vol. *12*(21), 3629. https://doi.org/10.3390/rs12213629

Métrich, N., Allard, P., Spilliaert, N., Andronico, D., & Burton, M. (2004). 2001 flank eruption of the alkali- and volatile-rich primitive basalt responsible for Mount Etna's evolution in the last three decades. *Earth and Planetary Science Letters*, *228*(1-2), 1–17. https://doi.org/10.1016/j.epsl.2004.09.036

Métrich, N., & Rutherford, M. J. (1998). Low pressure crystallization paths of H_2O-saturated Basaltic-Hawaiitic Melts from Mt Etna: Implications for open-system degassing of Basaltic Volcanoes. *Geochimica et Cosmochimica Acta*, *62*(7), 1195–1205. https://doi.org/10.1016/s0016-7037(98)00048-9

Michaud-Dubuy, A., Carazzo, G., & Kaminski, E. (2020). Wind entrainment in jets with reversing buoyancy: Implications for volcanic plumes. *Journal of Geophysical Research: Solid Earth*, *125*(10).

Mittal, T., & Delbridge, B. (2019). Detection of the 2012 Havre submarine eruption plume using Argo floats and its implications for ocean dynamics. *Earth and Planetary Science Letters*, *511*, 105–116. https://doi.org/10.1016/j.epsl.2019.01.035

Morton, B. R. (1962). Coaxial turbulent jets. *International Journal of Heat and Mass Transfer*, *5*(10), 955–965. https://doi.org/10.1016/0017-9310(62)90075-3

Morton, B. R. (1965). Modeling fire plumes. *Symposium (International) on Combustion*, *10*(1), 973–982. https://doi.org/10.1016/s0082-0784(65)80240-5

Morton, B. R., Taylor, G. I., & Turner, J. S. (1956). Turbulent gravitational convection from maintained and instantaneous sources. *Proceedings of the Royal Society of London - Series A: Mathematical and Physical Sciences*, *234*(1196), 1–23. https://doi.org/10.1098/rspa.1956.0011

Mueller, S. B., Houghton, B. F., Swanson, D. A., Poret, M., & Fagents, S. A. (2019). Total grain size distribution of an intense Hawaiian fountaining event: Case study of the 1959 Kilauea Iki eruption. *Bulletin of Volcanology*, *81*(7), 43. https://doi.org/10.1007/s00445-019-1304-y

Mulas, M., Cioni, R., Andronico, D., & Mundula, F. (2016). The explosive activity of the 1669 Monti Rossi eruption at Mt. Etna (Italy). *Journal of Volcanology and Geothermal Research*, *328*, 115–133. https://doi.org/10.1016/j.jvolgeores.2016.10.012

Parfitt, E. A. (1998). A study of clast size distribution, ash deposition and fragmentation in a Hawaiian-style volcanic eruption. *Journal of Volcanology and Geothermal Research*, *84*(3–4), 197–208. https://doi.org/10.1016/s0377-0273(98)00042-0

Parfitt, E. A., & Wilson, L. (1999). A Plinian treatment of fallout from Hawaiian lava fountains. *Journal of Volcanology and Geothermal Research*, *88*(1–2), 67–75. https://doi.org/10.1016/s0377-0273(98)00103-6

Pioli, L., Bonadonna, C., & Pistolesi, M. (2019). Reliability of total grain-size distribution of tephra deposits. *Scientific Reports*, *9*(1), 10006. https://doi.org/10.1038/s41598-019-46125-8

Poret, M., Corradini, S., Merucci, L., Costa, A., Andronico, D., Montopoli, M., et al. (2018). Reconstructing volcanic plume evolution integrating satellite and ground-based data: Application to the 23rd November 2013 Etna eruption. *Atmospheric Chemistry and Physics Discussion*(*18*, (7).4695–4714. https://doi.org/10.5194/acp-18-4695-2018

Poret, M., Costa, A., Andronico, D., Scollo, S., Gouhier, M., & Cristaldi, A. (2018). Modeling eruption source parameters by integrating field, ground-based, and satellite-based measurements: The case of the 23 February 2013 Etna Paroxysm. *Journal of Geophysical Research: Solid Earth*, *123*(7), 5427–5450. https://doi.org/10.1029/2017jb015163

Ricou, F. P., & Spalding, D. B. (1961). Measurements of entrainment by axisymmetrical turbulent jets. *Journal of Fluid Mechanics*, *11*(1), 21–32. https://doi.org/10.1017/s0022112061000834

Romero, J. E., Vera, F., Polacci, M., Morgavi, D., Arzilli, F., Alam, M. A., et al. (2018). Tephra from the 3 March 2015 sustained column related to explosive lava fountain activity at Volcán Villarrica (Chile). *Frontiers in Earth Science*, *6*, 98. https://doi.org/10.3389/feart.2018.00098

Rooney, G. G., & Linden, P. F. (1996). Similarity considerations for non-Boussinesq plumes in an unstratified environment. *Journal of Fluid Mechanics*, *318*, 237–250. https://doi.org/10.1017/s0022112096007100

Rossi, E., Bonadonna, C., & Degruyter, W. (2019). A new strategy for the estimation of plume height from clast dispersal in various atmospheric and eruptive conditions. *Earth and Planetary Science Letters*, *505*, 1–12. https://doi.org/10.1016/j.epsl.2018.10.007

Scollo, S., Boselli, A., Coltelli, M., Leto, G., Pisani, G., Prestifilippo, M., et al. (2015). Volcanic ash concentration during the 12 August 2011 Etna eruption. *Geophysical Research Letters*, *42*(8), 2634–2641. https://doi.org/10.1002/2015gl063027

Scollo, S., Boselli, A., Coltelli, M., Leto, G., Pisani, G., Spinelli, N., & Wang, X. (2012). Monitoring Etna volcanic plumes using a scanning LiDAR. *Bulletin of Volcanology*, *74*(10), 2383–2395. https://doi.org/10.1007/s00445-012-0669-y

Scollo, S., Coltelli, M., Bonadonna, C., & Del Carlo, P. (2013). Tephra hazard assessment at Mt. Etna (Italy). *Natural Hazards and Earth System Sciences*, *13*(12), 3221–3233. https://doi.org/10.5194/nhess-13-3221-2013

Scollo, S., Del Carlo, P., & Coltelli, M. (2007). Tephra fallout of 2001 Etna flank eruption: Analysis of the deposit and plume dispersion. *Journal of Volcanology and Geothermal Research*, *160*(1–2), 147–164. https://doi.org/10.1016/j.jvolgeores.2006.09.007

Scollo, S., Prestifilippo, M., Bonadonna, C., Cioni, R., Corradini, S., Degruyter, W., et al. (2019). Near-real-time tephra fallout assessment at Mt. Etna, Italy. *Remote Sensing*, *11*(24), 2987. https://doi.org/10.3390/rs11242987

Scollo, S., Prestifilippo, M., Pecora, E., Corradini, S., Merucci, L., Spata, G., & Coltelli, M. (2014). Eruption column height estimation of the 2011-2013 Etna lava fountains. *Annals of Geophysics*, *57*(2). https://doi.org/10.4401/ag-6396

Scollo, S., Prestifilippo, M., Spata, G., D'Agostino, M., & Coltelli, M. (2009). Monitoring and forecasting Etna volcanic plumes. *Natural Hazards and Earth System Sciences*, *9*(5), 1573–1585. https://doi.org/10.5194/nhess-9-1573-2009

Shampine, L. F., & Reichelt, M. W. (1997). The MATLAB ode suite. *SIAM Journal on Scientific Computing*, *18*(1), 1–22. https://doi.org/10.1137/s1064827594276424

Shampine, L. F., Reichelt, M. W., & Kierzenka, J. A. (1999). Solving Index-1 DAEs in MATLAB and Simulink. *SIAM Review*, *41*(3), 538–552. https://doi.org/10.1137/s003614459933425x

Spanu, A., de'Michieli Vitturi, M., & Barsotti, S. (2016). Reconstructing eruptive source parameters from tephra deposit: A numerical study of medium-sized explosive eruptions at Etna volcano. *Bulletin of Volcanology*, *78*(9), 59. https://doi.org/10.1007/s00445-016-1051-2

Sparks, R. S. J., Bursik, M. I., Ablay, G. J., Thomas, R. M. E., & Carey, S. N. (1992). Sedimentation of tephra by volcanic plumes. Part 2: Controls on thickness and grain-size variations of tephra fall deposits. *Bulletin of Volcanology*, *54*(8), 685–695. https://doi.org/10.1007/bf00430779

Sparks, R. S. J., Bursik, M. I., Carey, S. N., Gilbert, J., Glaze, L. S., Sigurdsson, H., & Woods, A. W. (1997). *Volcanic plumes*. John Wiley and Sons Ltd.

Spilliaert, N., Allard, P., Métrich, N., & Sobolev, A. V. (2006). Melt inclusion record of the conditions of ascent, degassing, and extrusion of volatile-rich alkali basalt during the powerful 2002 flank eruption of Mount Etna (Italy). *Journal of Geophysical Research*, *111*(B4). https://doi.org/10.1029/2005jb003934

Stothers, R. B., Wolff, J. A., Self, S., & Rampino, M. R. (1986). Basaltic fissure eruptions, plume heights, and atmospheric aerosols. *Geophysical Research Letters*, *13*(8), 725–728. https://doi.org/10.1029/gl013i008p00725

Suzuki, Y. J., & Koyaguchi, T. (2015). Effects of wind on entrainment efficiency in volcanic plumes. *Journal of Geophysical Research: Solid Earth*, *120*(9), 6122–6140. https://doi.org/10.1002/2015jb012208

Taddeucci, J., Edmonds, M., Houghton, b., James, M. R., & Vergniolle, S. (2015). Hawaiian and Strombolian eruptions. In H. Sigurdsson, B. Houghton, S. R. McNutt, H. Rymer, & J. Stix (Eds.), *The encyclopedia of volcanoes* (pp. 485–503). Elsevier. https://doi.org/10.1016/b978-0-12-385938-9.00027-4

Vulpiani, G., Ripepe, M., & Valade, S. (2016). Mass discharge rate retrieval combining weather radar and thermal camera observations. *Journal of Geophysical Research: Solid Earth*, *121*(8), 5679–5695. https://doi.org/10.1002/2016jb013191

Wilson, L., & Walker, G. P. L. (1987). Explosive volcanic eruptions–VI. Ejecta dispersal in plinian eruptions: The control of eruption conditions and atmospheric properties. *Geophysical Journal International*, *89*(2), 657–679. https://doi.org/10.1111/j.1365-246x.1987.tb05186.x

Woodhouse, M. J., Hogg, A. J., Phillips, J. C., & Sparks, R. S. J. (2013). Interaction between volcanic plumes and wind during the 2010 Eyjafjallajökull eruption, Iceland. *Journal of Geophysical Research: Solid Earth*, *118*(1), 92–109. https://doi.org/10.1029/2012jb009592

Woods, A. W. (1988). The fluid dynamics and thermodynamics of eruption columns. *Bulletin of Volcanology*, *50*(3), 169–193. https://doi.org/10.1007/bf01079681

Woods, A. W. (1993). A model of the plumes above basaltic fissure eruptions. *Geophysical Research Letters*, *20*(12), 1115–1118. https://doi.org/10.1029/93gl01215

Woods, A. W., & Bower, S. M. (1995). The decompression of volcanic jets in a crater during explosive volcanic eruptions. *Earth and Planetary Science Letters*, *131*(3–4), 189–205. https://doi.org/10.1016/0012-821x(95)00012-2

Woods, A. W., & Bursik, M. I. (1991). Particle fallout, thermal disequilibrium and volcanic plumes. *Bulletin of Volcanology*, *53*(7), 559–570. https://doi.org/10.1007/bf00298156